



# Unveiling the internal structure of the Hercules supercluster

R. Monteiro-Oliveira<sup>1,2,3</sup>★ D. F. Morell<sup>1,4</sup> V. M. Sampaio<sup>1,5</sup> A. L. B. Ribeiro<sup>2</sup> and R. R. de Carvalho<sup>5</sup>

<sup>1</sup> Academia Sinica, Institute of Astronomy and Astrophysics, 11F of AS/NTU Astronomy–Mathematics Building, No. 1, Section 4, Roosevelt Rd, Taipei 10617, Taiwan

<sup>2</sup> Universidade Estadual de Santa Cruz, Laboratório de Astrofísica Teórica e Observacional, 45650-000 Ilhéus, Bahia, Brazil

<sup>3</sup> Universidade de São Paulo, Inst. de Astronomia, Geofísica e Ciências Atmosféricas, Depto de Astronomia, R. do Matão 1226, 05508-090 São Paulo, Brazil

<sup>4</sup> Instituto de Astronomía Teórica y Experimental (CCT Córdoba, CONICET, UNC), Laprida 854, X5000BGR Córdoba, Argentina

<sup>5</sup> NAT – Universidade Cruzeiro do Sul / Universidade Cidade de São Paulo, 01506-000, São Paulo, Brazil

Accepted 2021 November 3. Received 2021 November 3; in original form 2021 August 19

## ABSTRACT

We have investigated the structure of the Hercules supercluster (SCL160) based on data originally extracted from the Sloan Digital Sky Survey (SDSS-DR7). We have traced the mass distribution in the field through the numerical density, weighted by the  $r'$  luminosity of the galaxies, and classified objects based on their spatial position and redshift. This has allowed us to address not only the kinematics of the supercluster as a whole, but also the internal kinematics of each cluster, which had not been explored further before. We have confirmed that the Hercules supercluster is composed of the galaxy clusters A2147, A2151, and A2152. A2151 consists of five subclusters, A2147 two, and A2152 at least two. They form the heart of the Hercules supercluster. We also have found two other gravitationally bound clusters, therefore increasing the known members of the supercluster. We have estimated a total mass of  $2.1 \pm 0.2 \times 10^{15} M_{\odot}$  for the Hercules supercluster. To determine the dynamical masses in this work, we have resorted to the  $M_{200}-\sigma$  scaling relation and the caustic technique. Comparing both methods with simulated data of bimodal merging clusters, we found that the caustic, as well as the  $\sigma$ -based masses, is biased through the merger age, showing a boost just after pericentric passage. This is not in line with the principle of the caustic method, which affirms it does not depend on the cluster dynamical state.

**Key words:** galaxies: clusters: general – galaxies: clusters: individual: A2147 – galaxies: clusters: individual: A2151 – galaxies: clusters: individual: A2152.

## 1 INTRODUCTION

Structures have been growing in the Universe since early times, driven by the gravitational force. Continuous growth started from initial density perturbations and then proceeded from the hierarchical merging of smaller bodies (e.g. Kravtsov & Borgani 2012). From a theoretical point of view, the process of structure formation can be described in terms of the density contrast parameter ( $\delta$ : e.g. Guth & Pi 1982). A key point to understanding how the Universe has evolved from  $\delta \approx 10^{-5}$  in the recombination epoch (Planck Collaboration et al. 2016) to the present  $\delta \approx 10^2$  as seen in galaxy clusters (e.g. More et al. 2011) is the presence of cold dark matter (CDM). Just after the beginning of the matter–energy equivalence epoch, baryons and photons were coupled, preventing any growth of baryon overdensities (Silk damping: Silk 1967, 1968). However, as CDM is not subject to this damping, the first structure seeds started to grow in the density field before the recombination epoch, when baryons finally started to fall into the pre-existing potential wells created by CDM condensation.

According to the hierarchical scenario, guided by  $\Lambda$ CDM cosmology, superclusters of galaxies constitute the next generation of virialized structures in the Universe, reaching masses  $\sim 10^{16} M_{\odot}$  (e.g.

Einasto et al. 2021) and extending across tens of Mpc (e.g. Bagchi et al. 2017). Currently, the top part of the mass function is occupied by galaxy clusters with masses  $10^{14}\text{--}10^{15} M_{\odot}$  (e.g. Kravtsov & Borgani 2012). The number of known superclusters has been increasing (e.g. Einasto et al. 1997; Chon, Böhringer & Nowak 2013; Chow-Martinez et al. 2014), despite some of them later being reclassified, since they will not collapse in the future (Chon & Böhringer 2015), e.g. the ex-superclusters Shapley (Scaramella et al. 1989) and Laniakea (Tully et al. 2014).

Superclusters of galaxies can provide us with a varied field of studies. For example, given the diversity of environments, ranging from poorly populated voids to the densest regions (e.g. Santiago-Bautista et al. 2020), superclusters are a good laboratory through which to study galaxy evolution (e.g. Krause, Ribeiro & Lopes 2013; Ribeiro et al. 2013; Guglielmo et al. 2018; Seth & Raychaudhury 2020; Kelkar et al. 2020), which is affected strongly by their environment. The morphology–density relation shows that galaxy types are not uniformly distributed in space (Dressler 1980). Red, quiescent, early-type galaxies are mainly found in high-density environments, while blue, star-forming, late-type galaxies tend to avoid such environments. Among different environmental quenching mechanisms such as starvation (van de Voort et al. 2017), ram-pressure stripping (RPS: Gunn & Gott 1972), and tidal mass loss (Johnston, Sigurdsson & Hernquist 1999), interaction/mergers between clusters can also be relevant to galaxy evolution. The most

\* E-mail: rogerionline@gmail.com

**Table 1.** X-ray-derived masses according to Piffaretti et al. (2011). The original  $M_{500}$  were translated into  $M_{200}$  supposing that the mass density can be described by a Navarro–Frenk–White (NFW) profile with a halo concentration given by Duffy et al. (2008).

Cluster	$\bar{\alpha}$ (J2000)	$\bar{\delta}$ (J2000)	$M_{200}$ ( $10^{14} M_\odot$ )	$R_{200}$ (Mpc)
A2147	240.5779	+16.0200	3.53	1.44
A2152	241.3842	+16.4420	0.81	0.88
A2151	241.7179	+17.7810	0.47	0.74

striking example is the bullet-cluster case, where there is a noticeable enhancement in the ram-pressure effect, which quickly removes a galaxy's gas component (e.g. Lourenço et al. 2020; Moura, Machado & Monteiro-Oliveira 2021). More recently, it has been considered that cosmic filaments also carry a considerable amount of angular momentum (Wang et al. 2021). Other peculiar features can be also found in some objects, such as the unusual mass concentration in the core of the Saraswati supercluster (Bagchi et al. 2017), which can call into question the predictions of modern cosmology.

The Hercules supercluster (SCL160: Einasto et al. 1997) was first mentioned in the literature by Shapley (1934), who noticed a galaxy overdensity in the direction of the Hercules constellation. Later, Cooke et al. (1977) and Tarenghi et al. (1979) stated that it is formed by the galaxy clusters A2151 ( $z = 0.0366$ , the ‘Hercules cluster’; Struble & Rood 1999), A2147 ( $z = 0.0350$ ; Struble & Rood 1999), and A2152 ( $z = 0.0410$ ; Struble & Rood 1999). In the following, we will introduce the particulars of each one. Their locations and respective X-ray mass estimations (Piffaretti et al. 2011) can be found in Table 1.

The galaxy cluster Abell 2151 (A2151) is located north of the field. Using data from *Einstein* Observatory, Magri et al. (1988) showed that A2151 has bimodal X-ray emission. In contrast to the hot gas, Bird, Dickey & Salpeter (1993) identified three kinematic subclusters, later (Bird, Davis & Beers 1995) called A2151N, A2151E, and A2151C. However, the X-ray emission is found to be located only in the central substructure (A2151C).

Taking the cluster as a single object, Escalera et al. (1994) estimated a virial mass of  $M_{\text{vir}} = 1.07 \pm 2.13 \times 10^{15} M_\odot$  inside a radius of  $1.95 \pm 0.14$  Mpc, based on radial velocities of only 79 galaxies. More recently, Agulli et al. (2016) updated this value to  $M_{200} = 4.0 \pm 0.4 \times 10^{14} M_\odot$  using the caustic technique and 360 members.

The internal structure of A2151 proved to be more complicated than previously hinted at. After a visual inspection of the projected galaxy distribution, Maccagni, Garilli & Tarenghi (1995) qualitatively suggested the presence of a fourth structure, A2151S, located to the south. Unfortunately, they did not perform any statistical procedure to classify the galaxies, only drawing straight arbitrary lines as subcluster borders. Lopes de Oliveira et al. (2010) showed that A2151S is not a fossil group as previously stated. They speculate that it could be part of A2151.

With improved X-ray observations by the *ROSAT* Position Sensitive Proportional Counter (PSPC), Bird et al. (1995) made it clear that subcluster A2151C is composed of two intracluster medium (ICM) substructures. Huang & Sarazin (1996) named them A2151C–B and A2151C–F, in reference to their relative brightness. Posterior analysis based on *ROSAT* High Resolution Imager (HRI: Huang & Sarazin 1996) and *XMM–Newton* data showed that A2151C–B is a cool core, implying it is a dynamically relaxed structure (e.g. Soja et al. 2018). Regarding the other subclusters, Bird et al. (1995)

and Huang & Sarazin (1996) agreed that A2151E has very weak emission, whereas A2151N and A2151S present no detectable X-ray emission (e.g. Doubrava et al. 2020; Monteiro-Oliveira et al. 2020).

The ambiguity in the optical and X-ray characterization makes A2151 an unsolved puzzle from the kinematic point of view. What dynamical scenario led the subclusters to the current configuration? Bird et al. (1995) proposed a partial explanation, where the eastern and central subclusters are seen in a post-merger phase due to gas absence in the former. However, they disregard the fact that A2151C's gas has a bimodal structure. Furthermore, they did not mention the role of A2151N and A2151S. Thereby, a full dynamical description involving all subclusters is still lacking in the literature.

In contrast to A2151, the galaxy cluster Abell 2147 (A2147) has not been intensively studied yet. Based on *Chandra* data, Sanderson, Ponman & O'Sullivan (2006) classified A2147 as a merger candidate, suggesting that it has many components. They also stated that there is no spatial coincidence between the brightest cluster galaxy (BCG) and the cluster potential well traced by the ICM. Zhang et al. (2011) found the offset to be 9.2 kpc. In line with previous findings, Hudson et al. (2010) classified A2147 as a non-cool core and a probable merger because of its elongated X-ray emission (Vikhlinin et al. 2009). However, its caustic structure does not differ from that of a single cluster (Wojtak & Łokas 2007).

Among the clusters, Abell 2152 (A2152) has been the most poorly studied regardless of the wavelength. According to Blakeslee et al. (2001), it forms a ‘double cluster’ along with A2147 because of their projected proximity. A2152 contains two BCGs (0.5 mag difference) 0.47 arcsec distant from each other (Blakeslee et al. 2001). The authors have suggested that the apparent offset between the first BCG and the X-ray peak (2.1 arcmin) is due to the misidentification of a background source. However, lacking high-resolution data, they were not able to answer this question.

As well as the internal structure of the clusters mentioned beforehand, the Hercules supercluster as a whole has not been much explored so far. A unique attempt to describe this large-scale structure was made by Barmby & Huchra (1998), who provided a kinematic view of the supercluster, but they considered the clusters as single ones whereas at least A2151 is clearly multimodal.

Were there more cluster members than those already stated? What is the total mass of the supercluster? These are some questions that we aim to fill in the present work. We have conducted an extensive study of the entire field of the Hercules supercluster, providing well-detailed anatomy including not only the previously identified members but also new candidates. We have identified the supercluster members, based not only on their galaxy projected distribution but also on their radial velocities. To accomplish these tasks, we resorted to the galaxy catalogue of Yang et al. (2007a), later improved by de Carvalho et al. (2017a). Having identified the clusters, we have computed their masses based on the galaxy dynamics. To do this, we have compared the power of two well-known methods: the scaling relation  $M_{200} - \sigma$  (e.g. Evrard et al. 2008; Munari et al. 2013) and the caustic (Diaferio & Geller 1997; Diaferio 1999). Finally, with the masses, we have obtained the kinematic description of each cluster. We also proposed a toy model for the supercluster as a whole.

This work is organized as follows. A data description is presented in Section 2. The mapping of the galaxy distribution can be found in Section 3, followed by the dynamical analysis in Section 4. The mass estimates of the structures identified are in Section 5. The cluster's internal kinematics are described in Section 6. We discuss the results of our analysis in Section 7 and summarize our findings in Section 8.

In this work, we adopt the standard  $\Lambda$ CDM cosmology, given by  $\Omega_m = 0.27$ ,  $\Omega_\Lambda = 0.73$ ,  $\Omega_k = 0$ , and  $h = 0.7$ .

## 2 DATA DESCRIPTION

Our sample is built using the Yang Catalog (Yang et al. 2007b), which applies a Halo Finder Algorithm (Yang et al. 2005) to the New York University Value Added Galaxy Catalog (Blanton et al. 2005). The original Yang Catalog is based on the Sloan Digital Sky Survey (SDSS) fifth data release (Brinchmann et al. 2004). However, here we use an updated version presented in de Carvalho et al. (2017b, hereafter dC17), which is based on SDSS-DR7 (de Carvalho et al. 2017b), and we next describe this in detail.

The dC17 catalogue is built by selecting all SDSS-DR7 galaxies within  $0.03 \leq z \leq 0.1^1$  and with apparent magnitude  $m_r \leq 17.78$ , which is the survey spectroscopic completeness limit at  $z = 0.1$ . The lower redshift bound is adopted to avoid bias in the stellar population parameter estimates due to the fixed 3-arcsec aperture used in the SDSS. Membership is then defined by applying a shiftgapper technique (see Lopes et al. 2009 for more details) to the galaxies with line-of-sight velocity and projected radial distance within the range  $\pm 4000 \text{ km s}^{-1}$  and  $d_{\text{proj}} \leq 2.5h^{-1} \text{ Mpc}$  (i.e.  $\sim 3.47 \text{ Mpc}$  for  $h = 0.7$ ), respectively, with respect to the clustercentric coordinates (RA, Dec., and redshift) described in the Yang Catalog.<sup>2</sup> The advantage of using the dC17 catalogue instead of the original SDSS data relies on the fact that the former is more complete, bringing complementary information on galaxy stellar populations (e.g. age, metallicity, stellar mass, among others). This wealth of information provides opportunities for further investigations: for example, how these properties can be correlated with the cluster merger phase.

We retrieved the catalogue of all Yang groups located in a circular region with radius of  $3^\circ$  centred on  $\alpha, \delta = (240.57792, +16.020)$ . This region is large enough to encompass the three main constituents of the Hercules supercluster, A2147, A2151, and A2152, as well as other possible companion groups.

The so-called Hercules catalogue is comprised by 1259 galaxies within the interval  $8490 \text{ km s}^{-1} \leq v \leq 14690 \text{ km s}^{-1}$ <sup>3</sup>, or equivalently  $0.02832 \leq z \leq 0.04899$ . In Fig. 1, we present the respective redshift distribution. The Hercules cluster is located in the nearby Universe, which allows a deeper completeness limit in luminosity,  $M_{r,\text{com}}$ . In this work we adopt the limit established in dC17 for structures with  $z \leq 0.04$ , namely  $M_r \leq -18.40$ .

## 3 MAPPING THE GALAXY DISTRIBUTION

The cluster's galaxy content is embedded in a large dark matter halo that corresponds to  $\sim 80$  per cent of the cluster total mass, whereas the former accounts only for  $\sim 5$  per cent. However, despite some bias being present, the integrated stellar light is a good tracer of the cluster total mass. In this sense, we employed the projected galaxy distribution to map the mass allocation along the Hercules field, using the sample selected in Section 2.

To translate the discrete galaxies into a smoothed map (e.g. Wen & Han 2013), we split the field into squared cells of 1 arcmin<sup>2</sup> inside

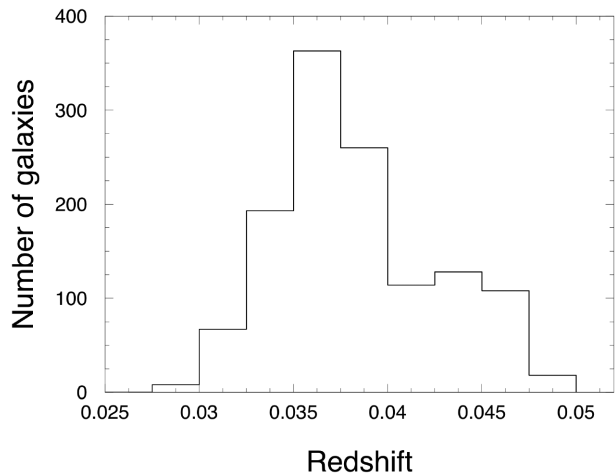


**Figure 1.** Redshift distribution of the 1259 galaxies in the Hercules catalogue.

which we computed the numerical density,

$$D(\xi) = \sum_{i=1}^N K(\xi_i, \sigma_\xi) L_i, \quad (1)$$

representing a sum over all  $N$  galaxies located inside a radius of  $\sigma_\xi$ , the smoothing scale. In case we want to weight the map by the  $r'$  luminosity, we adopt

$$L_i = 10^{-0.4(M_{r_i} - M_{r,\text{com}})}, \quad (2)$$

whereas  $L_i = 1$  if we want to compute only the single numerical density. Then,  $L_i$  is convoluted by the Epanechnikov kernel,

$$K(\xi_i, \sigma_\xi) = \begin{cases} \frac{3}{4} \left[ 1 - \left( \frac{\xi_i}{\sigma_\xi} \right)^2 \right], & \xi_i \leq \sigma_\xi, \\ 0, & \xi_i > \sigma_\xi. \end{cases} \quad (3)$$

We computed both the numerical density and the luminosity-weighted map. The results can be seen in Fig. 2, where a smoothing scale of 9 arcmin was adopted. Importantly, the final map does not change significantly if an alternative scale within a few arcmin is adopted instead.

Overall, the two maps are very similar to each other, presenting roughly the same complex scenario. By definition, the numerical density map highlights the density contrast, emphasizing the borders. On the other hand, the luminosity-weighted map is more efficient in enhancing the substructures. As this is a piece of vital information for our purposes, we choose to use this map henceforth. Despite the majority of galaxies appearing to be related to the clusters A2147, A2151, and A2152, they present themselves an intricate multimodal structure. Whereas A2151 is relatively isolated in the north, A2147 and A2152 are close to each other, being connected through a bridge. The main clusters are surrounded by another four galaxy clumps (A–D).

To identify the most prominent galaxy clumps and therefore the most massive regions, we have employed a tailor-made algorithm. It works by searching for the local maxima within a moving circular region of 3-arcmin radius. Then, the peak centre position is defined as the pixel-weighted mean inside this circular region. The uncertainty in each peak position was set as 50 kpc. To determine the noise level, we resampled the map 10 000 times (allowing repetition), taking the standard deviation after each iteration and the overall mean  $\sigma_n$  at the end. The significance of each peak detection,  $S$ , was defined as the

<sup>1</sup>This limit refers to the mean redshift of the selected group/cluster. Then, the underlying members were selected in a slice comprising galaxies within  $\pm 4000 \text{ km s}^{-1}$ .

<sup>2</sup>We highlight that clustercentric coordinates are the only information we use from the Yang Catalog.

<sup>3</sup>We adopted  $v = cz$ .

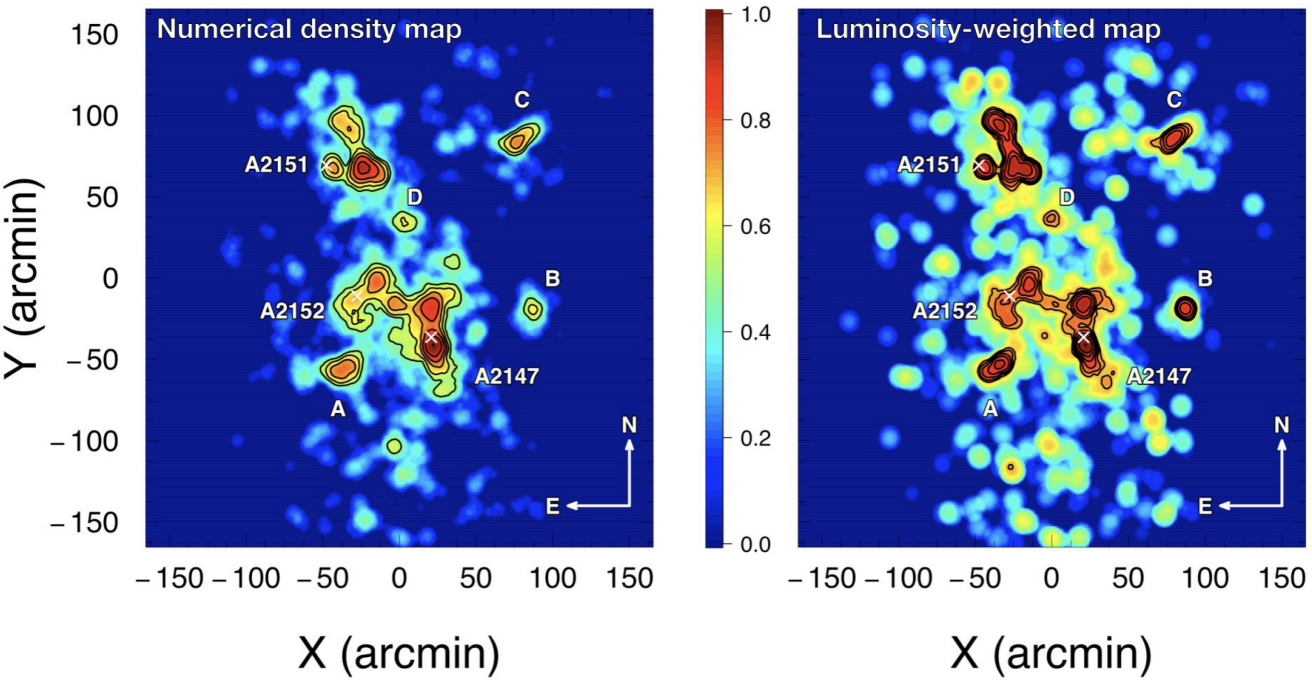


**Figure 2.** Galaxy distribution in the Hercules supercluster. All values are normalized by the maximum pixel in the respective map. *Left:* numerical projected density map. *Right:* numerical density weighted by  $r'$  luminosity. In both maps, the crosses represent the cluster location according to the X-ray catalogue of Piffaretti et al. (2011). Another four noteworthy clumps are labelled A–D.

ratio between the local maxima value and the noise level  $\sigma_n$ . After this procedure, we found 14 high-density regions above the threshold  $S > 10\sigma_n$ , as we can see in Fig. 3.

There are five meaningful peaks in the area of A2151, encompassing the four known members (#2, #4, #5, and #10) plus a candidate (#13). In A2147, there are two structures (#1 and #3) and three others are found in A2152 (#8, #11, and #12). In the same region, a peak is located at the bridge (#14) and surrounding A2152 (#6). As previously stated, another two satellites are also found (#7 and #9).

After finding the supercluster's backbone, our forthcoming analysis aims to investigate the role of these mass clumps in the internal dynamics of each galaxy cluster, as well as to check whether the surrounding clumps A–D are bound to the aforementioned clusters or constitute independent structures.

#### 4 DYNAMICAL ANALYSIS

Despite the large area covered ( $\sim 28$  deg $^2$ ), we will focus on the densest part of the field where the virialized regions are expected to be. With this approach, we do not want to take into account sparse galaxies, whose unique contribution is to add noise in the galaxy cluster membership assignment, distracting the reader from the goal of describing the main cluster substructures, their internal dynamics and large-scale kinematics.

We have selected all galaxies inside a radius of 1.1 Mpc ( $\sim 24$  arcmin) from each clump introduced in Fig. 3. A visual inspection ensured that no spatial bias was added, as this would potentially lead to the detection of a non-physical structure in the field. For the sake of organization, we will refer to three regions hereafter: (1) A2151 + D, (2) A2152 + A2147 + A, and (3) B + C. To avoid contamination by galaxies belonging to any neighbour structure, the  $3\sigma_v$ -clipping procedure (Yahil & Vidal 1977) was applied in each region to remove outliers.

To proceed with galaxy membership assignment inside the regions, we resort to the Gaussian multidimensional mixture modelling MCLUST (Scrucca et al. 2016), implemented in the R package (R Core Team 2014). In general terms, the algorithm searches for optimized clusters from models encompassing variable shapes, orientations, and volumes. For a detailed description of the application of MCLUST in galaxy classification, we refer the reader to the recent works of Morell et al. (2020) and Lourenço et al. (2020).

We have applied MCLUST in its three-dimensional mode, having as input the spatial coordinates plus the radial velocity of each galaxy. Despite being allowed by MCLUST, no informative prior was given. The most credible model for galaxy classification, i.e. the number of groups and the corresponding galaxy membership, was chosen after the Bayesian information criterion (BIC: Kass & Raftery 1995).<sup>4</sup> However, the classification of each galaxy is not a unique quantity and there is an uncertainty attributed by MCLUST, as we can see in Fig. 4. To define whether a given galaxy is a member of some group, we have considered a maximum of 25 per cent uncertainty in its classification. This choice has been proved to offer a good compromise between the final number of galaxies in each group and the consistency of the dynamical mass obtained, as we will describe in more detail in Section 5.

The final classification is shown in Fig. 5. 3D-MCLUST confirms the complexity of the Hercules field. Each region is itself formed by multiple groups, which we will refer to henceforth as subclusters. Of note, the majority of galaxy clumps identified in Section 3 are also related to dynamical structures. In the following, we will discuss the results for each region individually.

<sup>4</sup>It is very important to stress that MCLUST implements an opposite definition of BIC than largely found in the literature (e.g. Schwarz 1978). In the particular case of MCLUST, a larger BIC points in favour of the preferred model.

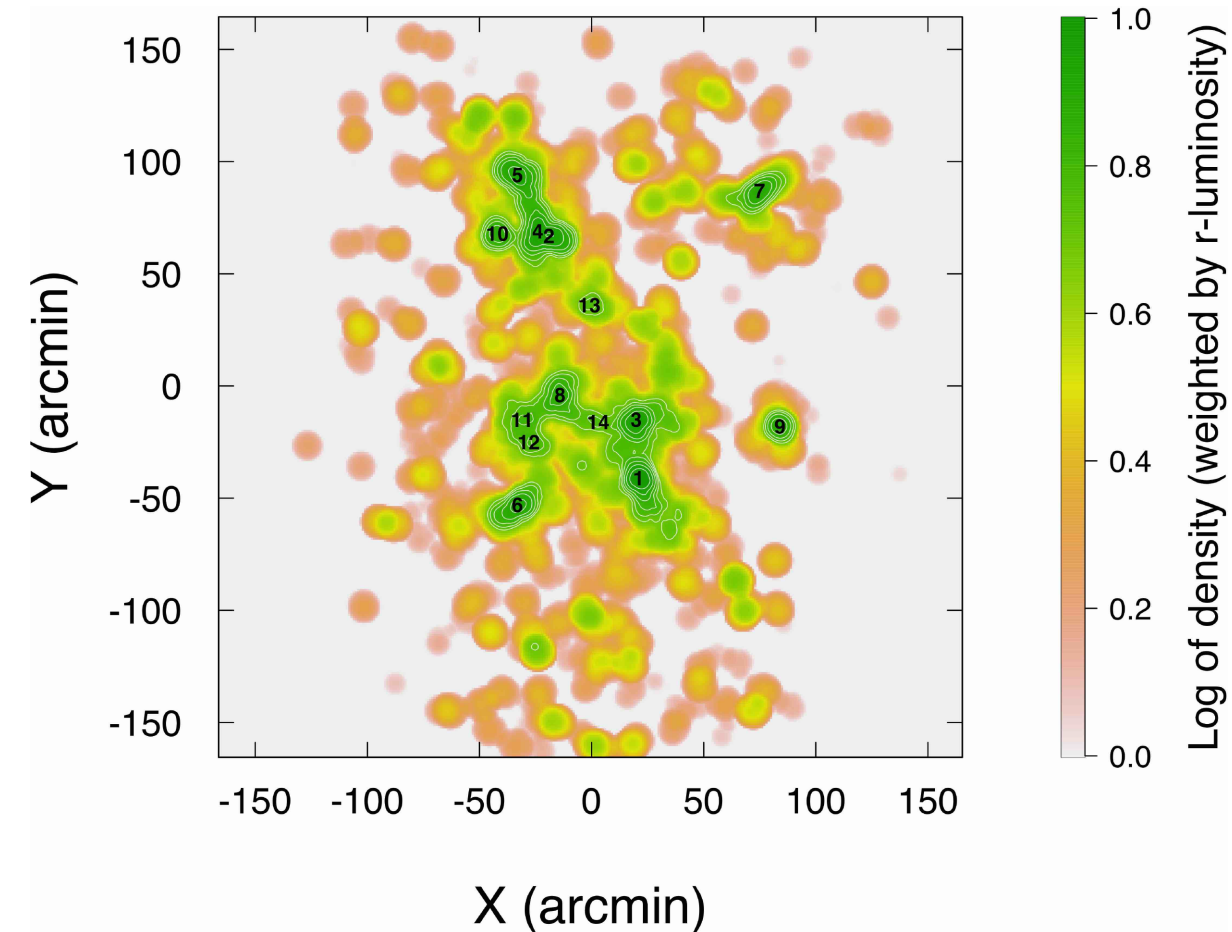


**Figure 3.** Mass peaks identified in the luminosity-weighted density map above the threshold  $10\sigma_n$ . The numbers show the ranked significance and are placed exactly at the corresponding peak centre. White contours are the same as in Fig. 2, right.

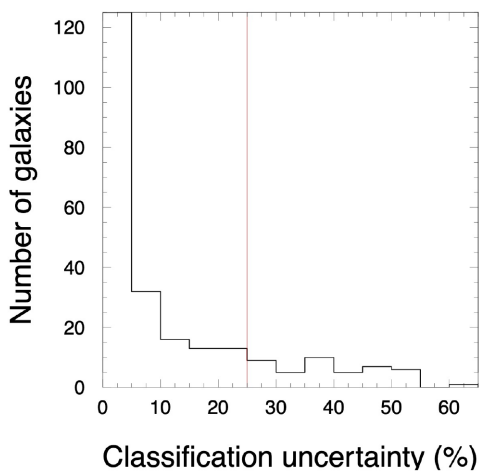


**Figure 4.** Uncertainty in the galaxy classification given by MCLUST for the region A2151 + D. In order to increase confidence in the subcluster membership assignment, our final sample only contains those galaxies for which classification was performed with an uncertainty of less than 25 per cent.

#### 4.1 A2151 + D

The galaxy cluster A2151 is comprised by (at least) three subclusters (e.g. Bird et al. 1993, 1995; Maccagni et al. 1995), previously called

A2151N, A2151E, and A2151C, according to their position. Later, Huang & Sarazin (1996) found that the central one is not a single but a bimodal system, comprised by A2151C–B and A2151C–F.<sup>5</sup> A fifth structure (labelled ‘D’ in Fig. 2) was called A2151S by Huang & Sarazin (1996) and Sánchez-Janssen et al. (2005), but the authors have not stated any strong argument to ensure that clump is indeed part of A2151. Later, we will provide definitive proof regarding this matter after checking whether it is bounded with the A2151 main bodies.

The 199 selected galaxies are characterized by  $\bar{z} = 0.0364 \pm 0.0027$  and  $\sigma_v/(1+\bar{z}) = 794^{+43}_{-37}$  km s<sup>-1</sup>. According to the Anderson–Darling test, the radial velocity distribution can be described by a Gaussian function within 95 per cent confidence level (c.l.;  $p$ -value = 0.10).

In its best model, 3D-MCLUST identified six groups. The second-best model ( $\Delta\text{BIC} = 1^6$ ) also pointed to six sets, with minimum changes concerning the first model. Five of those groups are

<sup>5</sup>B and F stands for bright and faint, respectively, and are related to their X-ray emission.

<sup>6</sup>According to Kass & Raftery (1995), the model criteria for selection from  $\Delta\text{BIC} = \text{BIC}_{\text{major}} - \text{BIC}_{\text{minor}}$  are as follows:  $\Delta\text{BIC} = 1$ –2: the models are comparable,  $\Delta\text{BIC} = 2$ –6: positive evidence in favour of the model with largest BIC,  $\Delta\text{BIC} = 6$ –10: strong evidence,  $\Delta\text{BIC} > 10$ : very strong evidence.

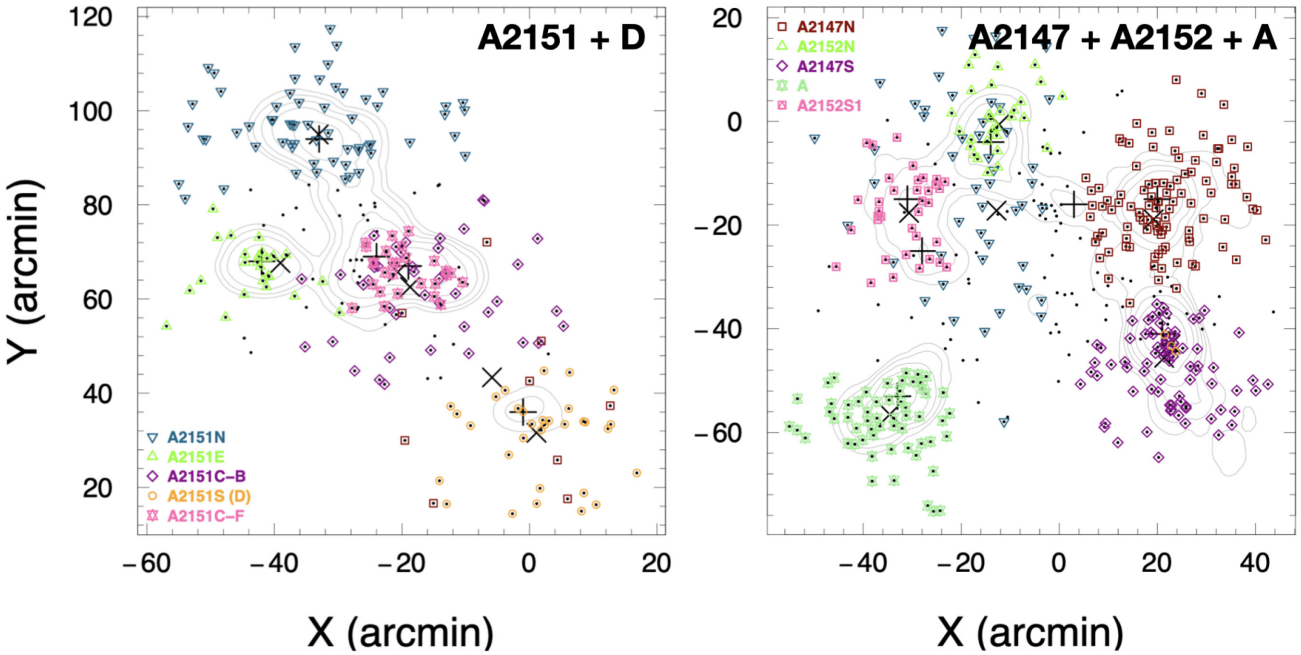


**Figure 5.** 3D-MCLUST classification. Black dots alone (i.e. not overlaid with any other symbol) correspond to galaxies with uncertainty in classification greater than 25 per cent, and therefore not considered for dynamical analysis. *Left:* A2151 + D. *Right:* A2147 + A2152 + A. The same coordinate convention as in Fig. 3 was adopted. Plus signals mark the overdensity peaks as identified in Fig. 3 and crosses identify the group centroids as calculated by 3D-MCLUST.

**Table 2.** Substructures of A2151.  $\alpha$  and  $\delta$  refer to the peaks identified in the luminosity-weighted map.

Subcluster	$\alpha$ (J2000)	$\delta$ (J2000)	$N_{\text{gals}}$	$z$	$\sigma_v/(1+\bar{z})$ (km s $^{-1}$ )	$M_{200}-\sigma$		Caustic	
						$M_{200}$ ( $10^{14} M_\odot$ )	$R_{200}$ (kpc)	$M_{200}$ ( $10^{13} M_\odot$ )	$R_{200}$ (kpc)
A2151N	241.49354	18.19872	62	$0.0374 \pm 0.0013$	$404^{+25}_{-22}$	$0.62^{+0.12}_{-0.11}$	$809^{+48}_{-51}$	$0.95^{+0.19}_{-0.30}$	$964^{+79}_{-94}$
A2151E	241.65275	17.76490	25	$0.0391 \pm 0.0014$	$415^{+24}_{-25}$	$0.65^{+0.12}_{-0.12}$	$823^{+48}_{-56}$	$0.69^{+0.27}_{-0.36}$	$871^{+124}_{-147}$
A2151C-B	241.24956	17.74695	43	$0.0363 \pm 0.0012$	$358^{+20}_{-25}$	$0.43^{+0.09}_{-0.10}$	$716^{+45}_{-60}$	$0.68^{+0.30}_{-0.15}$	$864^{+63}_{-150}$
A2151S (D)	240.93730	17.22772	32	$0.0342 \pm 0.0016$	$471^{+29}_{-27}$	$0.97^{+0.19}_{-0.17}$	$938^{+58}_{-59}$	$1.13^{+0.47}_{-0.41}$	$1021^{+183}_{-117}$
A2151C-F	241.33708	17.78069	28	$0.0327 \pm 0.0009$	$280^{+18}_{-18}$	$0.20^{+0.04}_{-0.04}$	$558^{+38}_{-38}$	$0.34^{+0.04}_{-0.13}$	$683^{+37}_{-87}$

correlated straightforwardly with the mass overdensities identified in Section 3 (crosses in Fig. 5 indicate the peak positions). A full description of the subcluster properties so far can be seen in Table 2. They follow, within 95 per cent c.l. ( $p$ -value  $> 0.10$ ), a Gaussian distribution.

The remaining group has only seven galaxies that do not follow a Gaussian distribution ( $p$ -value = 0.018) within 95 per cent c.l. They are more spread out in the field than the others, sometimes overlapping with groups related to A2151S and A2151C-B. Two reasons make us believe that these galaxies are probably infalling into A2151's core: the absence of a corresponding mass clump and the non-Gaussianity of their members. We therefore did not consider these galaxies in the forthcoming analysis.

#### 4.2 A2147 + A2152 + A

The Southern part of the Hercules supercluster has been poorly studied in the optical so far. This field is dominated by the galaxy clusters A2147 and A2152, with a bright SZ-emitting bridge connecting them (Planck Collaboration et al. 2013). Despite some earlier studies of the Hercules supercluster (e.g. Barmby & Huchra 1998; Blakeslee et al.

2001) considering those clusters as single structures, the photometric analysis of Flin & Krywult (2006) has suggested that A2147 and A2152 are bimodal, which is in reasonable agreement with our finds in Section 3. We have found no mention of structure 'A' in the literature.

3D-MCLUST points to an unquestionable scenario with seven dynamical components. The reason for this statement is that the model mentioned is strongly favoured over the second-best model (five groups), as settled by the high  $\Delta\text{BIC} = 16$ . Notably, most of the galaxies located in the bridge were not classified according to our selection criteria.

Of the seven mass clumps, two were not correlated to any dynamical group: clump #14 at the bridge and #12, in the southernmost part of A2152. On the other side, two dynamic groups are not straightforwardly linked with any mass clump. However, one of them has only three galaxies and therefore was disregarded. The second one has 49 galaxies nearly overlaid with A2152 but also spread along the region between the two clusters. This group is characterized by  $\bar{z} = 0.0451 \pm 0.0012$ ,  $\sigma_v/(1+\bar{z}) = 375 \pm 25$  km s $^{-1}$ , and, with 95 per cent c.l., the radial velocities follow a Gaussian ( $p$ -value = 0.13). Its centroid is located midway between A2152N and the mass clump #14. The lack of evidence prevents us from proposing a unique

**Table 3.** Substructures of A2147 and A2152.  $\alpha$  and  $\delta$  refer to the peaks identified in the luminosity-weighted map.

Subcluster	$\alpha$ (J2000)	$\delta$ (J2000)	$N_{\text{gals}}$	$\bar{z}$	$\sigma_v/(1+\bar{z})$ (km s $^{-1}$ )	$M_{200}-\sigma$		Caustic	
						$M_{200}$ (10 $^{14}$ M $_{\odot}$ )	$R_{200}$ (kpc)	$M_{200}$ (10 $^{13}$ M $_{\odot}$ )	$R_{200}$ (kpc)
A2147N	240.57737	16.37394	100	$0.0375 \pm 0.0034$	$1021^{+60}_{-76}$	$10.10^{+1.89}_{-2.01}$	$2048^{+121}_{-146}$	$7.66^{+0.17}_{-1.32}$	$1937^{+13}_{-118}$
A2147S	240.56362	15.93999	81	$0.0353 \pm 0.0024$	$713^{+42}_{-47}$	$3.43^{+0.72}_{-0.69}$	$1430^{+94}_{-103}$	$3.32^{+0.88}_{-0.35}$	$1463^{+119}_{-53}$
A2152N	241.16792	16.56102	29	$0.0451 \pm 0.0012$	$375^{+21}_{-22}$	$0.48^{+0.10}_{-0.09}$	$743^{+50}_{-51}$	$0.60^{+0.25}_{-0.20}$	$832^{+141}_{-56}$
A2152S1	241.46462	16.37852	36	$0.0441 \pm 0.0010$	$294^{+18}_{-18}$	$0.24^{+0.05}_{-0.04}$	$585^{+39}_{-39}$	$0.28^{+0.18}_{-0.10}$	$646^{+149}_{-33}$
A	241.50144	15.74458	58	$0.0400 \pm 0.0023$	$690^{+41}_{-43}$	$3.10^{+0.59}_{-0.55}$	$1381^{+83}_{-87}$	$2.92^{+0.81}_{-0.41}$	$1407^{+120}_{-69}$

**Table 4.** Substructures B and C.  $\alpha$  and  $\delta$  refer to the peaks identified in the luminosity-weighted map.

Subcluster	$\alpha$ (J2000)	$\delta$ (J2000)	$N_{\text{gals}}$	$\bar{z}$	$\sigma_v/(1+\bar{z})$ (km s $^{-1}$ )	$M_{200}-\sigma$		Caustic	
						$M_{200}$ (10 $^{14}$ M $_{\odot}$ )	$R_{200}$ (kpc)	$M_{200}$ (10 $^{13}$ M $_{\odot}$ )	$R_{200}$ (kpc)
B	239.46532	16.31289	30	$0.0369 \pm 0.0012$	$356^{+21}_{-21}$	$0.42^{+0.09}_{-0.08}$	$708^{+47}_{-51}$	$0.55^{+0.15}_{-0.13}$	$807^{+70}_{-65}$
C	239.59758	18.06715	41	$0.0464 \pm 0.0013$	$374^{+23}_{-24}$	$0.49^{+0.10}_{-0.11}$	$745^{+47}_{-58}$	$0.82^{+0.14}_{-0.27}$	$925^{+50}_{-117}$

explanation for its nature, but it is probably comprised of a mixture of galaxies from the bridge and A2152.

The dynamical description of clusters A2147 and A2152 as well as mass clump A can be found in Table 3. We have named the southern fully characterized substructure of A2152 as A2152S1. All of them have their radial distributions described by a Gaussian with 95 per cent c.l. ( $p$ -value  $> 0.22$ ). Beyond providing us with a way to describe the internal kinematics of the clusters, these results will allow us to determine at what level the mass clump A is or is not related to the main body of the Hercules supercluster.

### 4.3 B + C

The last two structures of the Hercules field are further apart from the supercluster's core (A2147 + A2151 + A2152). Both B and C have a members' radial velocity distribution following a Gaussian distribution within 95 per cent c.l., with  $p$ -values being respectively 0.31 and 0.50. More details regarding the subcluster dynamics can be found in Table 4.

## 5 MASS ESTIMATES

### 5.1 $M_{200}-\sigma$ scaling relation

The first approach we have applied to estimate subcluster masses is based on the scaling relation between  $\sigma$ , the velocity dispersion of their member galaxies, and the host halo mass  $M_{200}$ . We have adopted the well-known scaling relation (Biviano et al. 2006; Evrard et al. 2008; Munari et al. 2013):

$$\frac{\sigma}{\text{km s}^{-1}} = A_{\text{ID}} \left[ \frac{h(z) M_{200}}{10^{15} \text{ M}_{\odot}} \right]^{\alpha}, \quad (4)$$

and we consider  $\sigma = \sigma_v/(1+\bar{z})$ ,  $A_{\text{ID}} = 1177 \pm 4.2 \text{ km s}^{-1}$  and  $\alpha = 0.364 \pm 0.0021$ , in agreement with Munari et al. (2013).

However, such a scaling relation is derived from simulated data, and therefore some bias could be added into  $M_{200}$ . Additionally, some bias contribution could come from observation restrictions, such as the small number of galaxies and the truncated cluster radius observed. In Ferragamo et al. (2020), the authors suggested a set of corrections to improve the mass estimation given by

equation (4). The procedure starts by correcting  $\sigma$  for small galaxy samples:

$$\sigma' = \sigma(N_{\text{gal}}) \left\{ 1 + \left[ \left( \frac{D}{N_{\text{gal}} - 1} \right)^{\beta} + B \right] \right\}, \quad (5)$$

where  $\sigma'$  is the non-biased estimator of the velocity dispersion,  $N_{\text{gal}}$  is the number of galaxies,  $D = 1/4$ ,  $B = -0.0016 \pm 0.0005$ , and  $\beta = 1$ .

In the next step,  $\sigma'$  should be corrected by multiplicative factors that account for the aperture radius where  $\sigma(N_{\text{gal}})$  is measured ( $f_1$ ), the fraction of massive galaxies present in the sample ( $f_2$ ), and the contamination by interlopers ( $f_3$ ). Since we do not have any information a priori about  $R_{200}$ , we choose  $f_1 = 0.998 \pm 0.001$ , which corresponds to members enclosed within  $R_{200}$ ,<sup>7</sup>  $f_2 = 0.99 \pm 0.01$  corresponding to a fraction of 50–100 per cent of massive galaxies, and  $f_3 = 1.05 \pm 0.01$ , supposing that the sample is contaminated by  $\sim 5$  per cent of interlopers (Wojtak et al. 2007).

Finally, the estimated mass should also itself be corrected by the effect of the finite sample:

$$M'_{200} = M_{200}(\sigma'') \left[ \frac{1 - E'\alpha}{(E'\alpha)^2(N_{\text{gal}} - 1)^{\gamma'}} + F' \right]^{-1}, \quad (6)$$

where  $M_{200}(\sigma'')$  is the biased estimator of the virial mass (equation 4),  $E' = 1.53 \pm 0.03$ ,  $F' = 1$ , and  $\gamma' = 1.11 \pm 0.04$ .

### 5.2 Caustic

The second approach to estimate the subcluster masses is the caustic technique developed by Diaferio & Geller (1997) and Diaferio (1999). This method is particularly relevant, as it provides a reliable way to measure the mass profile in galaxy groups and clusters, making no assumptions about the dynamical state and simply providing the galaxy celestial coordinates and redshifts. For example, Serra et al. (2011) showed that the caustic technique can recover the mass profile with better than 10 per cent accuracy in the range

<sup>7</sup>Actually, this factor ranges within a small interval [0.973, 1.044]. The uncertainty, however, presents a larger spread, as expected, ranging from 0.001 at  $1R_{200}$  to 0.128 at  $0.2R_{200}$ .

$(0.6\text{--}4)R_{200}$ . Furthermore, it provides a means of interloper removal (e.g. Serra, Angus & Diaferio 2010) and identification of cluster substructures (e.g. Yu et al. 2015).

Assuming a spherically symmetric system, the escape velocity can be related to the potential  $\phi$  as

$$v_{\text{esc}}^2 = -2\phi(r).$$

As we can only measure the line-of-sight (l.o.s) velocity component, we have  $\langle v_{\text{esc}}^2 \rangle = \langle v_{\text{esc,los}}^2 \rangle g(\beta)$ , where  $\beta$  is the anisotropy parameter and

$$g(\beta) = \frac{3 - 2\beta(r)}{1 - 2\beta(r)}.$$

Therefore, the cumulative total mass is

$$GM(< r) = r^2 \frac{d\phi}{dr} = -\frac{r}{2} \langle v_{\text{esc,los}}^2 \rangle g(\beta) \left( \frac{d \ln \langle v_{\text{esc,los}}^2 \rangle}{d \ln r} + \frac{d \ln g}{d \ln r} \right).$$

The equation above poses two problems, first, we must know  $\beta(r)$ , which is not generally the case, and secondly, the measurement of  $\langle v_{\text{esc,los}}^2 \rangle$  can be noisy owing to the presence of background and foreground galaxies. As found by Diaferio & Geller (1997), the latter can be bypassed by measuring the amplitude  $A(r)$  of the caustics (Kaiser 1987; Regos & Geller 1989) in the cluster projected phase space (PPS), representing the average component along the l.o.s. of the escape velocity. The mass profile is then

$$GM(< r) = \int_0^r A^2(r) F_\beta(r) dr,$$

where  $F_\beta(r) = F(r)g(\beta)$  and  $F(r) = -2\pi G\rho(r)r^2/\phi(r)$ . Diaferio & Geller (1997) also found that, in hierarchical clustering scenarios,  $F(r)$  is not a strong function of  $r$ . Furthermore,  $F_\beta(r)$  is also a slowly changing function of  $r$ , and can be therefore taken as a constant in the equation above:

$$GM(< r) = F_\beta \int_0^r A^2(r) dr.$$

To locate the caustic surfaces, one must apply a kernel density estimation to the tracers of the PPS of the projected radii and velocities. Diaferio (1999) uses an adaptive Gaussian kernel method, whereas Gifford, Miller & Kern (2013) use a standard fixed multidimensional Gaussian kernel that adapts independently to the sampling, according to Silverman (1986), and show that it recovers the cluster mass estimates with low scatter and bias. Then, the threshold  $\kappa$  that defines the caustic location, chosen by minimizing the quantity  $|\langle v_{\text{esc,los}}^2 \rangle - 4\langle v_{\text{los}}^2 \rangle|^2$  inside  $R_{200}$ , can be determined.

Some authors claimed  $F_\beta$  to be in the range 0.5–0.7 (Diaferio 1999; Serra et al. 2011; Gifford et al. 2013) against numerical simulations. The assumption of a constant value can lead the caustic technique to overestimate the mass by up to 70 per cent at smaller radii (Serra et al. 2010). We follow the Gifford et al. (2013) recipe and use  $F_\beta = 0.65$  and their proposed Gaussian kernel, through an implementation in the R statistical software. As found by Diaferio (1999), the most relevant systematic errors in the caustic technique are due to projection effects.

### 5.3 Results

The computed masses are presented in Table 2 for A2151 + D, in Table 3 for A2147 + A2152 + A, and in Table 4 for B + C. To estimate the errors in the caustic method, we have drawn 1000 resamplings of the subcluster centre position and then computed the mass. Each new centre was chosen from a Gaussian distribution with a mean equal to the known position and standard deviation equivalent

to its uncertainty (50 kpc). The PPS and the underlying caustic curves are illustrated in Fig. 6.

Within the error bars, both methods present comparable estimates. The total mass of each cluster, considering the sum of its respective subclusters, is  $2.88^{+0.31}_{-0.27} \times 10^{14} M_\odot$  for A2151,  $13.5^{+2.1}_{-1.7} \times 10^{14} M_\odot$  for A2147, and  $0.72^{+0.13}_{-0.10} \times 10^{14} M_\odot$  for A2152. These quantities were estimated by Barmby & Huchra (1998), taking each cluster as a single structure. The virial masses were  $7.0 \pm 0.9 \times 10^{14} M_\odot$ ,  $13.0 \pm 2.0 \times 10^{14} M_\odot$ , and  $7.2 \pm 1.7 \times 10^{14} M_\odot$  respectively for A2151, A2147, and A2152. Except for A2147, where there is good agreement, the other two estimates are higher than ours.

The internal energy of interacting clusters changes during the lifetime of a merger, leading to a temporary modification in their PPS. This effect is commonly seen as a boost in the cluster velocity dispersion in periods close to the pericentric passage (e.g. Pinkney et al. 1996; Takizawa, Nagino & Matsushita 2010; Monteiro-Oliveira et al. 2020), meaning that the masses obtained have to be considered with wariness. In fact, the comparison of dynamical-based masses with lensing-based ones is often considered an indicator of the cluster dynamical status (e.g. Soja et al. 2018; Monteiro-Oliveira et al. 2021).

## 6 KINEMATIC ANALYSIS

The Monte Carlo Merging Analysis Code (hereafter MCMAC-post) was introduced by Dawson (2013) and consists of an analytical description of the merger between two galaxy clusters. It determines the dynamical solutions for bounded haloes with mass density following NFW profiles (Navarro, Frenk & White 1996, 1997) truncated at  $R_{200}$ . The concentration parameter is fixed by the  $M_{200}-c_{200}$  scaling relation given by Duffy et al. (2008). For the sake of simplification, the collision is supposed to occur with no impact parameter and no angular momentum. However, a comparison with numerical simulations showed that all previous considerations play no significant effect on the final results (Dawson 2013). A typical merging configuration is illustrated in Fig. 7.

The code requires as input the halo masses, the projected distance between them<sup>8</sup> and their corresponding mean redshift. From these parameters, MCMAC-post makes their probability density functions generate plausible states of the two bodies' movement. A code extension presented in Andrade-Santos et al. (2015) (hereafter MCMAC-pre) also incorporates unbound solutions for pre-merger systems, i.e. the left term of the motion equation,

$$V_r^2 R_p \leq 2GM \sin^2 \alpha \cos \alpha, \quad (7)$$

is now allowed to be greater than the right side, where  $V_r$  is the radial velocity between the clusters,  $R_p$  their corresponding projected distance, and  $M$  the system total mass (Beers, Geller & Huchra 1982). However, MCMAC-pre additionally requires that  $V_r$  be less than the l.o.s. Hubble flow velocity. Then, the code defines the probability of a system being (un)bound as the ratio between the sum of the respective states assumed by equation (7) and the total number of realizations.

However, it is known that the uncertainties of the final results are relatively high because the exact geometry of the merger is not known a priori (angle  $\alpha$  in Fig. 7). A way to overcome this issue is to compute  $\alpha$  from the velocity components:

$$\alpha = \arctan \left( \frac{\delta v}{v_{\text{plane}}} \right), \quad (8)$$

<sup>8</sup>Computed as the separations of their respective luminosity-weighted peaks (Fig. 3).

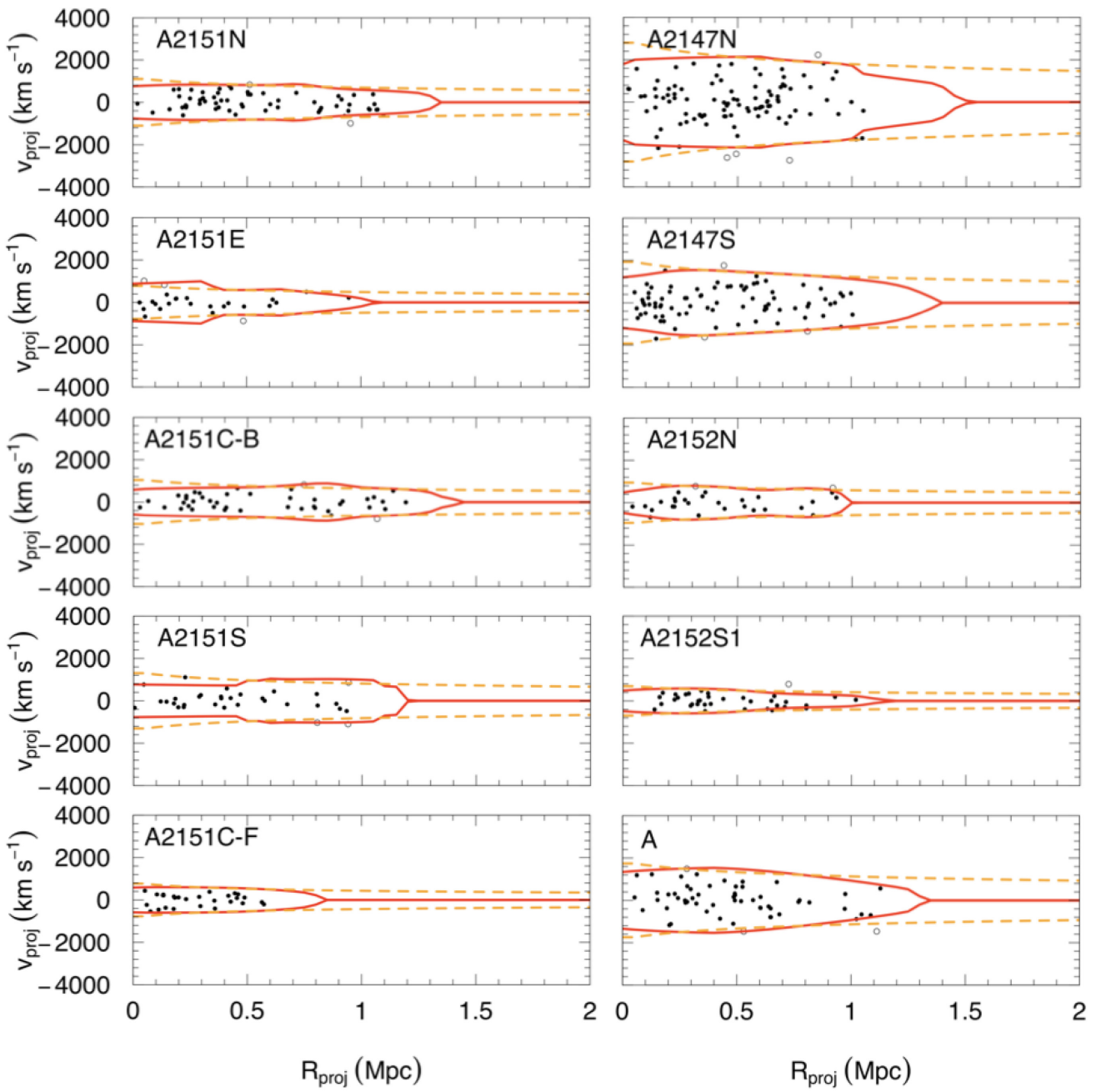


**Figure 6.** PPS of the groups identified through the 3D-MCLUST algorithm. Each plot contains only the galaxies assigned to their respective host group, as presented in Fig. 5. The projected velocity  $v_{\text{proj}}$  is computed for each  $i$ th galaxy as  $v_i - \bar{v}$  in the line of sight. The projected distance,  $R_{\text{proj}}$ , is measured in relation to the respective mass peak, as presented in Fig. 3. The continuous curve corresponds to the caustic profile and the dashed curve is the best NFW profile fit to the former and is a representation of the corresponding escape velocity surface. Filled points are considered as members of the groups, whereas open points are considered as interlopers.

where  $\delta v$  is the difference in velocity between the two clusters along the l.o.s., which comes from the data. Therefore, constraining  $v_{\text{plane}}$ , the relative velocity along the plane of the sky, we are directly restraining  $\alpha$ . Based on previous knowledge of cluster merger kinematics through hydrodynamical simulations (Springel & Farrar 2007; Machado & Lima Neto 2013; Machado et al. 2015; Doubrava et al. 2020; Moura et al. 2021), we adopted a uninformative prior  $v_{\text{plane}} < 1500 \text{ km s}^{-1}$ .

Our first goal is to determine what pairs are dynamically bound to each other, two by two, by running MCMAC-pre. The results are presented in Table 5. Then, we run MCMAC-post to unveil the

kinematics of each merger. The results can be seen in Table 6. In both cases, we have considered the mass from the  $M_{200}-\sigma$  scaling relation as the fiducial. We will discuss the merger scenarios in the following. We reinforce that all forthcoming results remaining comparable when we have considered the caustic mass as input in the MCMAC.

### 6.1 A2151

A summary of the A2151 structure is present in Fig. 8. The probability of each component being bound is shown in Fig. 8, right. Each of the four known components (N, E, C–B, and C–F) is linked

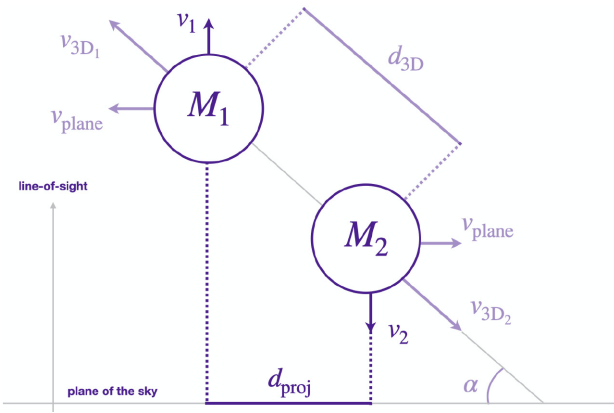


**Figure 7.** Typical configuration of a two-body system. The input quantities of MCMAC-post are highlighted: the halo masses ( $M_1$  and  $M_2$ ) and their mean redshift ( $\bar{z}$ ) as well as their projected separation ( $d_{\text{proj}}$ ). The corresponding three-dimensional quantities are not directly accessible, since we do not know the angle  $\alpha$  between the merger axis and the plane of the sky.

with at least one companion. Our analysis has shown that the southern clump ('D' in Fig. 2) is gravitationally bound with A2151C–F and A2151C–B, confirming, therefore, that A2151S is, in fact, part of the cluster A2151 as a whole.

With the exception of A2151E, which is linked only with A2151N, the other subsclusters form at least two bounded pairs each. A2151C–B is the most connected, being linked with A2151C–F, A2151S, and A2151N. Our find that A2151E and A2151C–F are not bounded is noteworthy. This conclusion excludes the previous conjecture of Bird et al. (1995), in which both consist of a post-merger system.

Due to the model's inability to discern between the pre- and post-merging states, we will describe both scenarios for the bounded pairs. The only relatively unquestionable fact is the pre-merger state between the central substructures, in the sense that the cool core of A2151C–B is still preserved (Laganá, Durret & Lopes 2019; Tiwari & Singh 2021). The encounter will be happening in  $0.38^{+0.12}_{-0.20}$  Gyr with a velocity of  $1147^{+169}_{-139}$  km s $^{-1}$  at a moderated distance of the plane of the sky ( $46^{+22}_{-19}$  degrees). At the apoapsis, both subclusters will be apart by  $1.47^{+1.1}_{-1.2}$  Mpc.

Other possible encounters would spend more than 1.6 Gyr taking place (for example, A2151N and A2151E), which is at least four times larger than the time of collision between the central structures A2151C–B and A2151C–F. Given this scenario, all other models involving one of the central subclusters consist of a toy model, since their dynamical state is going to change faster in comparison to the outskirts subclusters.

As justified before, we have excluded all pairs containing A2151C–B before running MCMAC-post. After that, only two pairs remain: N–E and S–C–F. It is important to remark that the post-merger scenario described by the code is degenerate, because it cannot point to which outgoing or incoming state is the most likely. Usually this degeneracy can be broken with multiwavelength observations (e.g. Ng et al. 2015; Monteiro-Oliveira et al. 2017b; Kim et al. 2021). However, our results point to a very unlikely incoming scenario for both pairs, because the time since the last collision (TSC<sub>1</sub>) is very large compared with the Hubble time. Therefore, this sketch was ruled out.

The outgoing post-merger scenario for A2151N–A2151E predicts that they had a pericentric passage  $1.6^{+0.4}_{-0.6}$  Gyr ago at  $1505^{+108}_{-92}$  km s $^{-1}$  with a merger axis aligned at  $28^{+13}_{-28}$  degrees with respect to the plane of the sky. The system would have already covered  $\sim 43$  per cent of the path to the apoapsis, where they can be found  $3.3^{+2.0}_{-2.1}$  Mpc

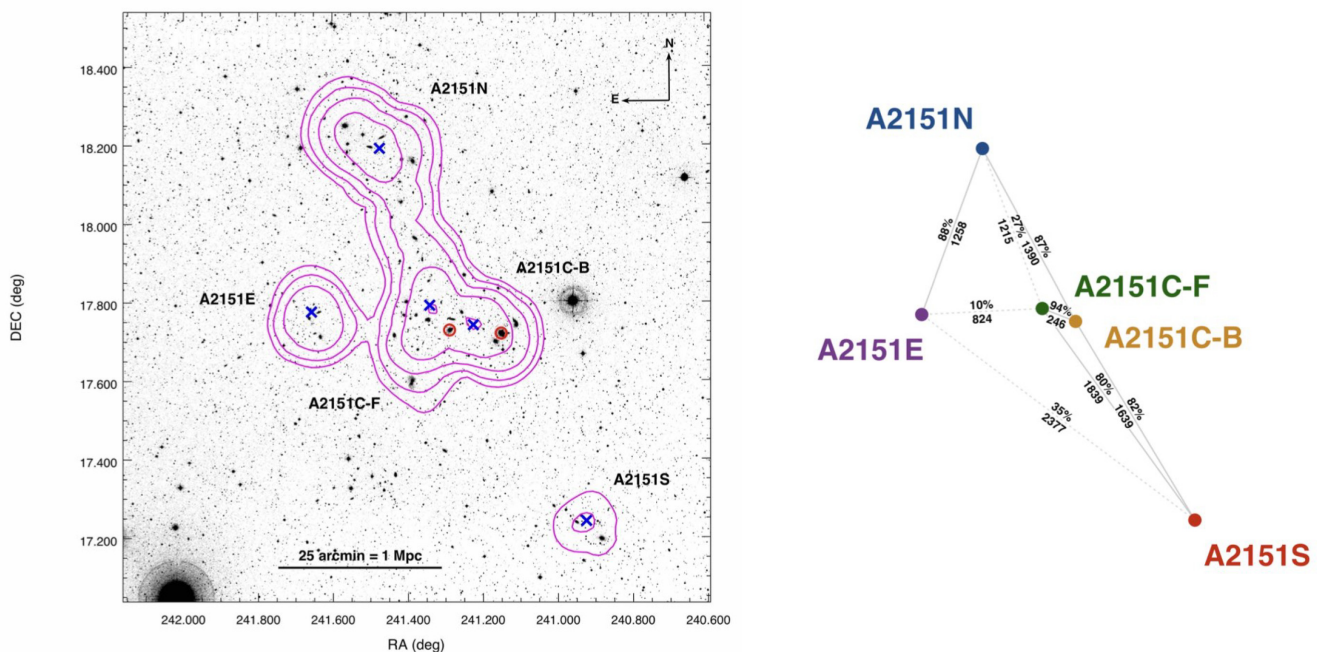


**Figure 8.** The galaxy cluster A2151 ( $\bar{z} = 0.0361 \pm 0.0024$ , a.k.a. Hercules cluster) and its main substructures. *Left:* luminosity-weighted map of the spectroscopic members (magenta contours) overlaid with optical DSS2-red ESO Online Digitized Sky Survey image. We found five significant galaxy clumps in this region (blue crosses), corresponding to A2151's subclusters. Only two of them (A2151C–B and A2151C–F) have measurable gas counterparts, whose X-ray emission peaks are marked with red circles. *Right:* A2151 skeleton. The respective distances among the clusters are shown in units of kpc. We also present the probability of each pair being bound (filled lines) as was obtained by the MCMAC-pre code.

**Table 5.** Dynamical description of the bound and pre-merger pairs according to MCMAC pre-output parameters.  $M$  is the cluster mass,  $z$  the mean redshift,  $d_{\text{proj}}$  the observed projected distance at apapsis,  $v_{\text{rad, obs}}$  the observed projected density,  $v_{\text{rad}}$ ,  $\alpha$  the merger angle,  $v_{3D, \text{obs}}$  the 3D observed velocity,  $d_{3D}$ ,  $\text{obs}$  the current 3D distance,  $d_{3D, \text{max}}$  the distance at apapsis, and  $TTC$  the time until collision.

Pre-merger pairs		C-B(1) – C-F(2)		S(1) – C-F(2)		Abell 2151		S(1) – C-B(2)		N(1) – E(2)		N(1) – C-B(2)	
		Median	68% c.l.	Median	68% c.l.	Median	68% c.l.	Median	68% c.l.	Median	68% c.l.	Median	68% c.l.
$M_{(1)}$	$10^{14} \text{ M}_\odot$	0.45	0.36–0.55	1.00	0.80–1.17	0.99	0.81–1.19	0.63	0.50–0.74	0.63	0.52–0.75		
$M_{(2)}$	$10^{14} \text{ M}_\odot$	0.20	0.17–0.25	0.20	0.17–0.24	0.44	0.34–0.54	0.66	0.54–0.77	0.44	0.34–0.54		
$z_{(1)}$	–	0.0352	0.0343–0.0360	0.0333	0.0233–0.0342	0.0353	0.0341–0.0363	0.0380	0.0369–0.0390	0.0370	0.0359–0.0379		
$z_{(2)}$	–	0.0334	0.0325–0.0341	0.0330	0.0321–0.0337	0.0357	0.0347–0.0367	0.0384	0.0374–0.0395	0.0367	0.0357–0.0376		
$d_{\text{proj}}$	Mpc	0.25	0.20–0.29	1.84	1.80–1.89	1.64	1.59–1.69	1.26	1.21–1.31	1.22	1.18–1.27		
$v_{\text{rad, obs}}$	km s $^{-1}$	547	348–801	182	1–259	217	1–305	235	2–327	203	0–287		
$\alpha$	degrees	46	27–68	29	0–41	30	0–43	30	0–43	28	0–41		
$v_{3D, \text{obs}}$	km s $^{-1}$	828	650–1121	449	291–676	522	329–765	549	361–833	511	300–750		
$d_{3D, \text{obs}}$	Mpc	0.36	0.21–0.48	2.10	1.75–2.47	1.89	1.55–2.25	1.46	1.19–1.75	1.38	1.15–1.65		
$v_{3D, \text{col}}$	km s $^{-1}$	1147	1008–1316	1564	1468–1666	1603	1510–1709	1508	1406–1609	1423	1333–1526		
$d_{3D, \text{max}}$	Mpc	1.47	0.27–2.57	4.99	1.84–8.14	4.56	1.62–7.60	3.38	1.25–5.51	3.17	1.22–5.14		
$TTC$	Gyr	0.38	0.18–0.50	2.77	1.66–3.54	2.20	1.34–2.87	1.63	0.98–2.09	1.66	0.99–2.11		
Pre-merger pairs		A2147S(1)–A2147N(2)		A2152S(1)–A2152N(2)		Abell 2152 + A2147 + A		A(1)–A2147S(2)		A(1)–A2152S(2)		A(1)–A2152S(2)	
$M_{(1)}$	$10^{14} \text{ M}_\odot$	3.45	2.73–4.17	0.24	0.19–0.29	3.15	2.58–3.74	3.22	2.64–3.80				
$M_{(2)}$	$10^{14} \text{ M}_\odot$	10.19	8.11–12.08	0.49	0.38–0.58	3.52	2.79–4.19	0.24	0.19–0.29				
$z_{(1)}$	–	0.0358	0.0335–0.0379	0.0444	0.0436–0.0452	0.0383	0.0363–0.0399	0.0425	0.0411–0.0437				
$z_{(2)}$	–	0.0366	0.0341–0.0392	0.0447	0.0439–0.0457	0.0373	0.0353–0.0389	0.0436	0.0427–0.0446				
$d_{\text{proj}}$	Mpc	1.19	1.14–1.23	0.93	0.88–0.98	2.53	2.48–2.57	1.74	1.69–1.79				
$v_{\text{rad, obs}}$	km s $^{-1}$	542	1–821	193	0–273	424	12–581	383	114–612				
$\alpha$	degrees	45	21–73	28	0–41	32	0–45	34	3–48				
$v_{3D, \text{obs}}$	km s $^{-1}$	947	3–1385	480	291–717	902	578–1295	789	513–1150				
$d_{3D, \text{obs}}$	Mpc	1.69	1.12–2.32	1.06	0.85–1.26	3.00	2.45–3.58	2.10	1.65–2.52				
$v_{3D, \text{col}}$	km s $^{-1}$	2830	2376–3351	1250	1153–1348	2601	2443–2757	2251	2090–2428				
$d_{3D, \text{max}}$	Mpc	2.75	1.15–4.31	2.45	0.91–3.90	7.43	2.55–12.42	5.46	1.71–9.14				
$TTC$	Gyr	0.99	0.38–1.35	1.38	0.82–1.76	2.03	1.22–2.59	1.65	0.95–2.14				

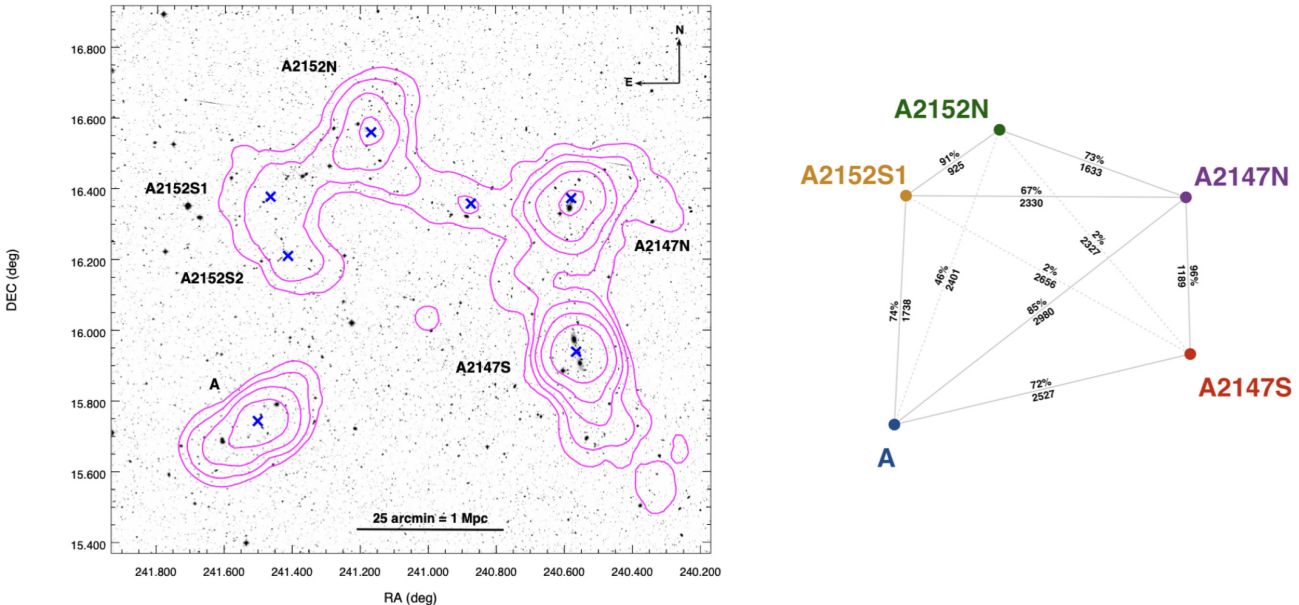


**Figure 9.** Same as Fig. 8, but now showing the region of A2147 + A2152 + A.

apart. For the system A2151S–A2151C–F, the encounter happened  $2.8^{+0.7}_{-1.1}$  Gyr ago at  $1563^{+101}_{-94}$  km s $^{-1}$ , which will lead to a maximum separation of  $4.8^{+2.8}_{-2.9}$  Mpc,  $\sim 44$  per cent of which has already been covered.

## 6.2 A2147 + A2152 + A

A zoomed view and the dynamical scheme are shown in Fig. 9. The clusters A2147 and A2152 have their internal substructures strongly bounded, with a probability larger than 90 per cent. The subcluster A2147N is the only one bounded with all other companions, which can be interpreted as a consequence of its dominant mass in the field. Regarding mass clump A, we confirm that it is part of the Hercules supercluster, being bounded with both clusters.

We will concentrate our discussion on the internal dynamics of each cluster and interactions involving clump A and its nearest neighbours (A2147S and A2152S1). In the pre-merger scenario, the subclusters of A2147 will have pericentric passage in  $0.99^{+0.36}_{-0.68}$  Gyr with a velocity of  $2830^{+521}_{-454}$  km s $^{-1}$  at a moderate collision axis ( $45^{+28}_{-24}$  degrees). For A2152, the values are respectively  $1.38^{+0.38}_{-0.56}$  Gyr,  $1250^{+98}_{-97}$  km s $^{-1}$ , and  $28^{+13}_{-28}$  degrees. The possible collision of A with A2147S would happen in  $2.03^{+0.56}_{-0.81}$  Gyr, with  $2601^{+156}_{-158}$  km s $^{-1}$  and  $32^{+13}_{-32}$  degrees, whereas the possible collision with A2152S1 is characterized by  $1.65^{+0.49}_{-0.70}$  Gyr,  $2251^{+177}_{-161}$  km s $^{-1}$ , and  $34^{+14}_{-31}$  degrees.

The elongated shape of X-ray emission in A2147 (e.g. Sanderson et al. 2006; Vikhlinin et al. 2009) is a hint that the system has already experienced a collision. In this case, if the system has been caught outgoing, the collision happened  $0.83^{+0.18}_{-0.27}$  Gyr ago, with  $2710^{+373}_{-510}$  km s $^{-1}$  and  $43^{+25}_{-24}$  degrees, the clusters having travelled a distance equivalent to 70 per cent of the path for the maximum separation at  $2.32^{+1.11}_{-1.12}$  Mpc. In the incoming scenario, the encounter would have occurred  $2.95^{+2.11}_{-1.90}$  Gyr ago.

The dynamical description of A2152 is a little bit less complicated, because the incoming scenario can be disregarded, since its related time is comparable to the Hubble one. Then, in the case in which the subclusters have already collided, this event happened  $1.36^{+0.36}_{-0.55}$  Gyr ago with an encounter velocity of  $1249^{+95}_{-98}$  km s $^{-1}$  along a merger

axis located  $28^{+12}_{-28}$  degrees from the plane of the sky. The subclusters have toured only 44 per cent of their path to reach the apoapsis at  $2.39^{+1.34}_{-1.48}$  Mpc.

## 7 DISCUSSION

### 7.1 Merger impact on dynamical mass estimation

The mergers of galaxy clusters involve energies up to  $10^{64}$  erg (Sarazin 2004), part of this amount being converted into internal movement of the galaxies. This energy transfer changes the PPS, leading to a temporary boost in the velocity dispersion near the pericentric passage (Pinkney et al. 1996). Hence, the question we ask is: how does this ephemeral disturbance bias dynamical-based mass estimations? Nevertheless, observations of a particular system only afford the description of a specific snapshot of the whole merger process. A proper answer to the question is not a simple task and the use of realistic computational simulations is a first step in addressing the issue, as they provide a follow-up over the time of interaction between the clusters (e.g. Roettiger, Burns & Loken 1996).

To address this inquiry, we have resorted to the Galaxy Cluster Merger Catalog, a suite of  $N$ -body and hydrodynamical simulations made publicly available by ZuHone & Kowalik (2016). The rich data set provides multiwavelength high-resolution simulations of the merger between two clusters over a timeline of 10 Gyr. To accomplish our goal and access the merger kinematics, we have considered the galaxy catalogue represented by dark matter particles of the simulation (projected position and redshift). Among several configurations, we choose the merger having a mass ratio of 1:3 ( $2.6 \times 10^{14} M_{\odot}$ ), with a null impact parameter ( $b = 0$  kpc) and with merger axis parallel to the plane of the sky ( $\alpha = 0$  degrees). This set-up covers most of the mergers we have characterized in Sections 5 and 6. For each snapshot, we have computed the masses in the same fashion as done in Section 5 using all the respective galaxies belonging to each cluster (i.e. the masses were measured from the same galaxies throughout the process). To check the reliability of this assumption, we tracked the galaxies inside  $R_{200}$ , and found that the numerical

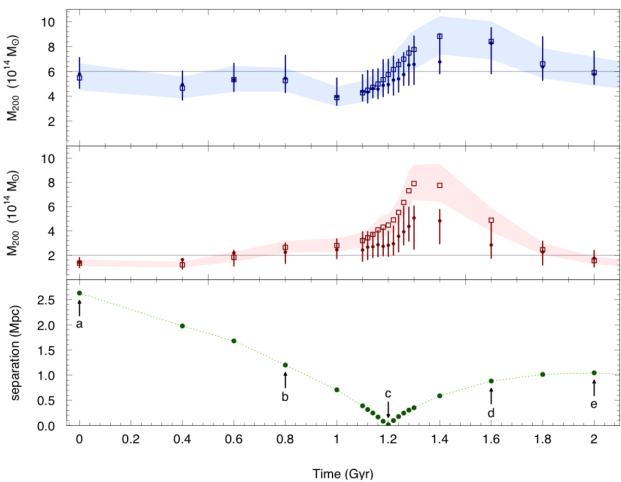


**Figure 10.** Evolution of the mass estimators across the timeline of a 1:3 mass ratio merger, with null impact parameter and a collision axis parallel to the plane of the sky. The main cluster ( $6 \times 10^{14} M_{\odot}$ ) and the subcluster ( $2 \times 10^{14} M_{\odot}$ ) are shown respectively in the upper (blue) and middle (red) panels. The  $M_{200} - \sigma$  value is represented by squares and the respective errors by a shadow area, whereas the caustic masses are marked by dots with error bars. At the bottom, we can see the cluster separation. We have defined five particular moments: (a) initial, (c) periaxis, (e) apoaxis, and two intermediate points (b and d), in which we compared the MCMAC predictions with the simulation results. A clear boost in the dynamical mass regardless the method can be seen between the instants c and e.

variation is less  $\sim 6$  per cent for the major cluster and  $\sim 1$  per cent for the minor, meaning an equivalent impact on the masses (e.g. Chiu et al. 2020). The resulting timeline is presented in Fig. 10.

As expected, the mass estimated from the velocity dispersion (equation 4; squares and shadow areas in the plot) shows a boost in the period between the periaxis (c) and the apoaxis (e). However, another unexpected fact is observed: the caustic-based estimation is also biased through the merger age. This find is not in line with what is largely accepted in the literature, that the caustic method is not dependent on the cluster dynamical state (e.g. Diaferio, Geller & Rines 2005; Geller et al. 2013). According to our results, the caustic mass behaviour is very similar to that from  $\sigma$ -based mass, though with subtle differences. In the less massive cluster, there is a suggestion that the use of the caustic method would provide a less biased measure even during the most acute merger phase (1–2 Gyr). However, even in this case, the estimated masses are  $\sim 2.5$  times higher than the real one but still lower than those from  $M_{200} - \sigma$ , which are biased  $\sim 4$  times higher.

It is beyond the scope of this work to provide an ultimate explanation for the observed behaviour of the caustic masses. Consequently, our take-home message is that both dynamical mass estimators are subjected to a boost near the pericentric passage and any kinematic analysis has to deal with this properly. However, we can speculate about the origin of caustic mass bias. Traditionally, to test its theoretical prediction of independence of the dynamical state, the caustic estimates are compared with weak lensing based masses, these being unquestionably free of any equilibrium assumption. For example, considering a sample of three galaxy clusters, Diaferio et al. (2005) found good agreement between both methods. With a larger sample (19), Geller et al. (2013) reached the same conclusion. However, a scrutiny of their dataset reveals that the majority (10) are clusters in some degree of interaction: A267 (substructured; Tucker et al. 2020), A1750 (pre-merger; Molnar et al. 2013), A1758 (post-

merger; Machado et al. 2015; Monteiro-Oliveira et al. 2017a), A1763 (sloshing; Douglass et al. 2018), A1835 (out of hydrostatic equilibrium; Ichikawa et al. 2013), A1914 (out of hydrostatic equilibrium; Mandal et al. 2019), A2034 (post-merger; Monteiro-Oliveira et al. 2018; Moura et al. 2021), A2142 (sloshing; Rossetti et al. 2013), A2219 (major merger; Canning et al. 2017), and A2631 (late stage of merger; Monteiro-Oliveira et al. 2021). Considering a multimodal structure as a single one will introduce a bias in the final mass, leading therefore to an unfruitful comparison. Another concern, recently presented by Chadayammuri et al. (2021), is that the halo concentration is another quantity susceptible to changes near the pericentric passage. This means that weak lensing masses assuming a parameterized NFW model can present overestimated results, because the model concentration assumes the values of relaxed clusters. Given this puzzling scenario, a more diligent comparison between caustic and weak lensing masses also has to consider the cluster dynamical state and/or the current merger phase.

Overall, it is important to state that our comparison with hydrodynamical simulations indicates that the bias in the caustic based mass occurs only during a short period of a cluster's life. Furthermore, the caustic technique still provides us with a confident estimate of the dynamical mass, even in the case where the cluster is interacting and possibly far from the equilibrium state.

Finally, we have compared our mass estimations with those available in the literature. The mass estimated by Tiwari & Singh (2021) for A2151C–B is  $1.3 \pm 0.8 \times 10^{14} M_{\odot}$  and that for A2151C–F is  $0.42 \pm 0.30 \times 10^{14} M_{\odot}$ . Both are consistent with our results within their error bars. As stated in the Introduction, no mass estimates were found for A2147 and A2152's subclusters, so we will compare them with the cluster total mass. Babyk, Del Popolo & Vavilova (2014), using *Chandra* data, have found  $10.93^{+1.27}_{-1.28} \times 10^{14} M_{\odot}$  for A2147, which is comparable with our estimate of the sum of the cluster constituents. In case of A2152, Piffaretti et al. (2011) found  $0.81 \times 10^{14} M_{\odot}$ , also in good agreement with our findings.

## 7.2 Accuracy of the kinematic description

The modelling of interactions among  $N > 2$  bodies is an expensive task even from the computational point of view. This is reflected in the small number of available studies involving more than two clusters (e.g. Brüggen, van Weeren & Röttgering 2012; Ruggiero et al. 2019; Doubrava et al. 2020). A strategy adopted to overcome such complexity is to start from a bimodal description and then to add a body acting as a ‘perturber’ (e.g. Doubrava et al. 2020). In the specific case of the present work, we can ask whether describing a complex system as a composition of interactions two by two could give us at least, a general idea of the chronological order of the collisions, as well as determining which bodies are bound to the others.

As the fiducial case, we have considered the triple merger in 1RXS J0603.3+4214 simulated by Brüggen et al. (2012). The initial conditions of the merger among the subclusters #1, #2 and #3 are presented in their table 1. We have used this information as input for MCMAC-pre. The slight difference, however, is the impact parameter, which originally ranged from 300–500 kpc but was assumed as null by MCMAC-pre, as described in Section 6. The original simulation shows that the collision between #1 and #2 happens  $\sim 1.3$  Gyr after the simulation starts at  $t = 0$  Gyr. Before that, however, a collision between #2 and #3 has happened at an unknown time. MCMAC-pre successfully recovers the bound state of the clusters. It is also efficient in describing the collision timeline, stating that #2–#3 will collide first at 0.7–1.4 Gyr and then #1–#2 at 1.2–2.3 Gyr, all within 68 per cent c.l. Of course, the simplicity of the

**Table 6.** Dynamical description of the post-merger pairs. Most of the parameters are the same as those in Table 5, but now including  $TSC_0$ , the time since pericentric passage for an outgoing system, where  $TSC_1$  is the time since pericentric passage for an incoming system,  $T$  the period between two successive collisions, and  $P$  the probability of observing the system.

Post-merger pairs		Abell 2151			
		Median	N(1)–E(2) 68% c.l.	Median	S(1)–C–F(2) 68% c.l.
$M_{(1)}$	$10^{14} M_\odot$	0.63	0.51–0.74	1.00	0.81–1.18
$M_{(2)}$	$10^{14} M_\odot$	0.66	0.54–0.77	0.20	0.16–0.24
$z_{(1)}$	–	0.0380	0.0369–0.0390	0.0333	0.0323–0.0343
$z_{(2)}$	–	0.0384	0.0375–0.0395	0.0330	0.0322–0.0338
$d_{\text{proj}}$	Mpc	1.26	1.21–1.31	1.84	1.79–1.88
$v_{\text{rad, obs}}$	km s $^{-1}$	229	0–323	188	2–266
$\alpha$	degrees	28	0–41	28	0–40
$v_{3D, \text{obs}}$	km s $^{-1}$	558	345–807	456	288–649
$d_{3D, \text{obs}}$	Mpc	1.43	1.17–1.68	2.09	1.77–2.45
$v_{3D, \text{col}}$	km s $^{-1}$	1505	1413–1614	1563	1469–1664
$d_{3D, \text{max}}$	Mpc	3.29	1.23–5.27	4.77	1.87–7.56
$TSC_0$	Gyr	1.60	0.97–2.01	2.75	1.65–3.45
$TSC_1$	Gyr	15.57	2.27–32.91	28.08	3.94–58.14
$T$	Gyr	17.71	4.20–35.56	31.34	7.66–62.48
$P$	%	21	0–35	19	0–33
Post-merger pairs		A2147S(1)–A2147N(2)		A2152S(1)–A2152N(2)	
		Median	68% c.l.	Median	68% c.l.
$M_{(1)}$	$10^{14} M_\odot$	3.46	2.75–4.16	0.24	0.19–0.29
$M_{(2)}$	$10^{14} M_\odot$	10.20	8.38–12.35	0.49	0.39–0.59
$z_{(1)}$	–	0.0356	0.0334–0.0377	0.0444	0.0436–0.0453
$z_{(2)}$	–	0.0368	0.0343–0.0398	0.0447	0.0438–0.0456
$d_{\text{proj}}$	Mpc	1.19	1.14–1.24	0.93	0.88–0.98
$v_{\text{rad, obs}}$	km s $^{-1}$	698	3–984	194	0–276
$\alpha$	degrees	43	19–68	28	0–40
$v_{3D, \text{obs}}$	km s $^{-1}$	1204	666–1668	490	304–722
$d_{3D, \text{obs}}$	Mpc	1.63	1.11–2.05	1.06	0.86–1.25
$v_{3D, \text{col}}$	km s $^{-1}$	2710	2200–3083	1249	1151–1344
$d_{3D, \text{max}}$	Mpc	2.32	1.20–3.43	2.39	0.91–3.73
$TSC_0$	Gyr	0.83	0.56–1.01	1.36	0.81–1.72
$TSC_1$	Gyr	2.95	1.05–5.06	12.73	1.89–25.70
$T$	Gyr	3.80	2.00–6.30	14.56	3.51–27.77
$P$	per cent	43	18–68	21	0–36

approach does not allow us to describe the full history of collisions, but it gives a good overview of the initial events and their timeline.

Another fundamental question we can ask is whether our kinematic analysis is trusted, given the merger impact on the mass determination. Or, in other words, does the MCMAC recover the correct physics of the merger even having as input possible biased masses? To address this question, we have chosen five snapshots in the Galaxy Cluster Merger Catalog subset described in Section 7.1 (labelled *a*–*e* in Fig. 10). Then we calculated the (sub)cluster masses (via a scaling relation, as in Section 5) and used them as input for MCMAC. In the end, we compared the outputs with the simulation predictions. The results can be seen in Table 7.

The MCMAC successfully recovered the gravitationally bound state for each pair with more than 95 per cent probability. Regarding its accuracy, we were only able to compare  $\alpha$ ,  $TTC/TSC_0$ , and  $d_{3D, \text{max}}$  since the Galaxy Cluster Merger Catalog does not provide further information about the mock galaxies. Overall, the MCMAC results agree within 68 per cent confidence level. The same conclusions can be drawn for the execution of MCMAS using no prior constraint in the  $v_{\text{plane}}$ , but the final results have larger error bars. Specifically talking about the time prediction, the MCMAC predictions can be considered in general as an upper limit of the ‘real’ events.

### 7.3 A2151

Despite this system being the subject of many works, none of them provided a full description of the entire cluster. We found that the Hercules cluster is comprised of five subclusters: two centrally located and the other three in the periphery. However, the X-ray emission is concentrated in the central part. A2151C–B hosts a still-untouched bright cool core, surrounded by A2151C–F. The first encounter between them will happen relatively soon, in 0.4 Gyr. Also, the conjecture of Tiwari & Singh (2021) that A2151C–F is a cluster in formation is supported by our analysis. In this work, we have confirmed quantitatively that A2151S is part of the Hercules cluster, being gravitationally bound with it.

We definitely discarded the scenario proposed by Bird et al. (1995) in which A2151E and A2152C–F form a post-merger system, as our analysis has shown that those clusters are not gravitationally bound to each other. In spite of it being a plausible scenario, we do not believe that the other subclusters have already experienced a merger, given the absence of a perturbed ICM in the field. Therefore, we suggest that A2151 as a whole is a cluster in an early stage of formation.

**Table 7.** Comparison between the simulation predictions and the scenario recovered by MCMAC in five specific moments. We also considered the MCMAC results with and without a prior in the relative cluster velocity along the plane of the sky.

Quantity	Unit	Sim.	MCMAC (w/ prior)	MCMAC (w/o prior)
			68 per cent c.l.	68 per cent c.l.
<i>a</i>				
$\alpha$	deg	0	0–37	12–65
$d_{3D, \text{max}}$	Mpc	2.6	2.6–8.8	2.6–8.6
TTC	Gyr	1.2	1.2–2.5	1.2–5.0
<i>b</i>				
$\alpha$	deg	0	0–39	8–62
$d_{3D, \text{max}}$	Mpc	2.6	1.2–2.4	1.1–3.2
TTC	Gyr	0.4	0.6–1.1	0.5–1.7
<i>c</i>				
$\alpha$	deg	0	0–42	3–59
$d_{3D, \text{max}}$	Mpc	1.0	0.2–0.7	0.0–0.6
TTC	Gyr	0	0.0–0.1	0.0–0.3
<i>d</i>				
$\alpha$	deg	0	0–35	4–55
$d_{3D, \text{max}}$	Mpc	1.0	0.9–1.5	0.8–2.0
$TSC_0$	Gyr	0.4	0.5–0.8	0.3–1.1
<i>e</i>				
$\alpha$	deg	0	0–32	5–56
$d_{3D, \text{max}}$	Mpc	1.0	1.1–1.9	1.0–2.4
$TSC_0$	Gyr	0.8	0.5–0.9	0.4–1.4

#### 7.4 A2147

We have presented the first description of the internal structure of A2147. This bimodal cluster is the most massive in the field, with a total mass of  $\sim 13.5 \times 10^{14} M_\odot$  (e.g. Pandge et al. 2019). The two subclusters, A2147N and A2147S, are 1.2 Mpc apart from each other (relative to their respective mass/luminosity peaks).

With the background of previous X-ray studies (e.g. Hudson et al. 2010; Lau et al. 2012; Laganá et al. 2019), there is strong evidence that A2147 as a whole is out of equilibrium. The presence of an offset of  $\sim 140$  kpc (Laine et al. 2003) between the ICM distribution mapped by its X-ray emission and the BCG (e.g. Käfer et al. 2019) is commonly referred to as a proxy of a post-merger system. However, this information alone does not allow us to distinguish between the post-merger outgoing and incoming scenarios. We suggest, though, that the outgoing one is more likely, as the collision happened only 0.8 Gyr ago, against 3.0 Gyr for the returning scenario. After such a long time, the observed optical–X-ray offset might vanish.

#### 7.5 A2152

We have made a significant advance in the comprehension of the internal structure of A2152, despite some questions that still remain open. One is the discrepancy between the mass distribution showing three concentrations while the dynamical structure shows only two structures, with a third one overlapped with both A2152N and A2152S1. We conjecture two scenarios: (1) the presence of two concentrations in the projected density map (Fig. 3) could be an effect of the smooth scale adopted and (2) the inability to detect a dynamical counterpart could be because the groups have a small separation along the line of sight. Regarding (1), a simple change of the smoothing scale to 11 arcsec can vanish the bimodality and

locate only one peak midway. About (2), any 3D mixture model will fail to classify galaxies in groups with similar redshift properly.

We have two plausible scenarios for the merging in A2152, both involving a time-scale of  $\sim 1.4$  Gyr (a pre-merger and an outgoing post-merger). To remove this degeneracy, another proxy is necessary. Blakeslee et al. (2001) reported an offset between the BCG and the peak of the ICM distribution, but they did not interpret this as a cluster merger signature. Our kinematic analysis of A2152N and A2152S1 pointed out that the merger events will happen/have happened with a small collision axis, in the sense that a possible detachment between the gas and the visible components (e.g. BCG) would be detectable. We therefore do not disregard the possibility that the observed offset is real and indicates that A2152 is a post-merger system with its components heading to the apoapsis.

#### 7.6 Hercules supercluster kinematics

After the description of each cluster’s inner structure, we turn our attention to the Hercules supercluster as a whole. To do this, we have considered all clusters as single structures, the total mass of which is concentrated at the corresponding mass centre. We also included the three surrounding structures, A, B, and C, and, using MCMAC-pre, investigated the degree of connection in the supercluster. The result is presented in Fig. 11.

Our analysis confirms that A2147, A2151, and A2152 are bound to each other. In contrast, Barmby & Huchra (1998) have found that the pair A2147–A2152 is not bound, even though, due to their projected proximity and the presence of a filament connecting them, we strongly suggest that A2147–A2152 are in fact bound, forming the heart of the Hercules supercluster.

Beyond these members, we found other three companion structures in the field. The kinematic analysis has proved that A and B are part of Hercules, as they are gravitationally bound with at least one other member. We have shown that they are single clusters with no signal of substructuring. A search on the NASA/IPAC Extragalactic Database (NED) reported the presence of the galaxy cluster MSPM 00022 at  $z = 0.03942$  (Smith et al. 2012) within a projected distance of 8.3 arcmin from A. The same authors report another galaxy cluster, MSPM 00080, at  $z = 0.03682$  only 2.06 arcmin away from B. We believe that both correspond to our findings, this work being the first one including them as Hercules members. On the other hand, the structure labelled C is not bound with any other member, therefore not belonging to the Hercules supercluster.

As the most massive member, A2147 has the largest number of connections, and it probably will work as a potential well for future gravitational collapse among all other structures. We estimate the total Hercules mass as  $2.1 \pm 0.2 \times 10^{15} M_\odot$ , obtained as a sum of the members’ individual masses (Tables 2, 3, and 4). This is somewhat lower than proposed by Barmby & Huchra (1998) ( $7.6 \pm 2.0 \times 10^{15} M_\odot$ ), but unfortunately the authors do not provide the radius at which they computed the masses of the clusters, making a direct comparison not feasible.

The Hercules supercluster encompasses an approximately linear region of  $\sim 9$  Mpc, being comparatively smaller than other known systems such as the A2142 supercluster (50 Mpc; Einasto et al. 2015), Ursa Major (50 Mpc; Krause et al. 2013), Coma (100 Mpc; Seth & Raychaudhury 2020), and Saraswati (200 Mpc; Bagchi et al. 2017), for example. We have shown the presence of a ‘bridge’, a filamentary structure connecting the northern part of A2147 and A2152. A galaxy concentration is also reported to be located within it (peak #14 in Fig. 3). This configuration resembles the same as seen in the system A3017/A3016 (Parekh et al. 2017; Foëx et al. 2017; Chon et al.

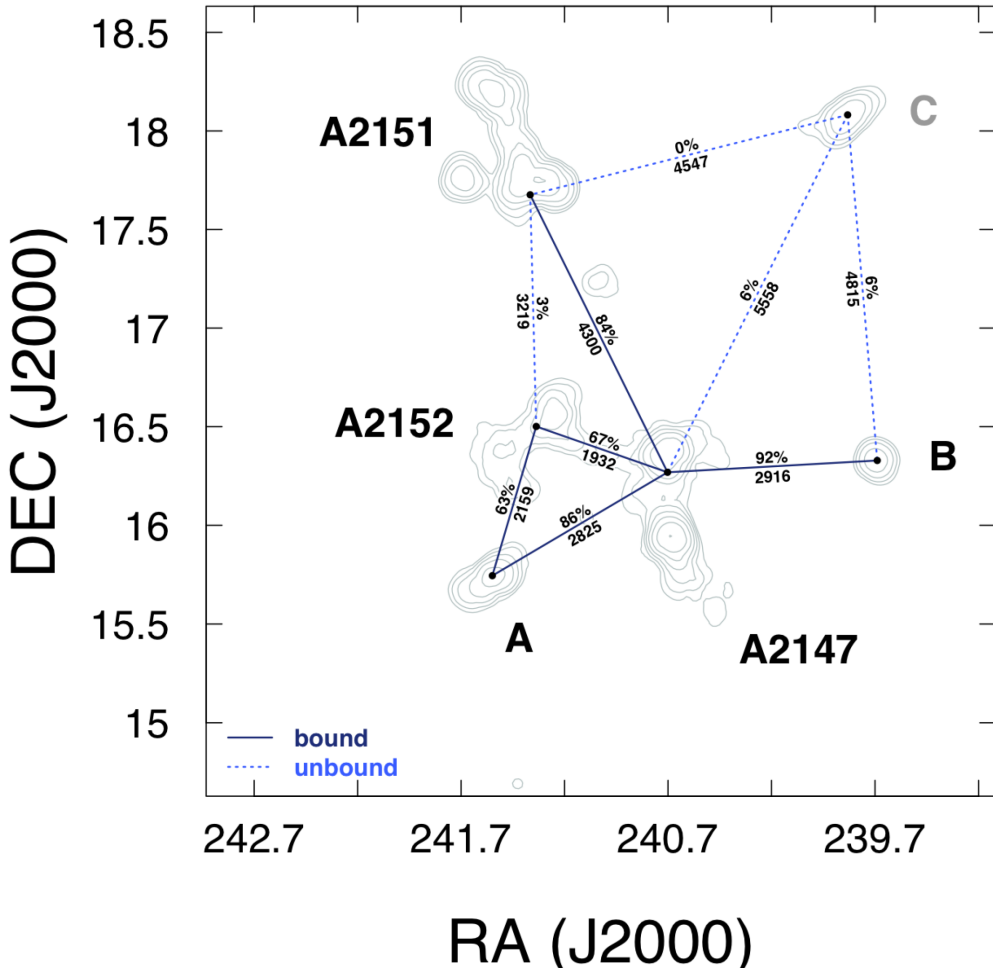


**Figure 11.** Skeleton of the Hercules supercluster (SCL160) and the dynamic connection among the structures. Besides the previously known members, A2147, A2151, and A2152, we have identified in this work two others, labelled A and B. Straight lines stand for bound pairs and dashed lines for unbound ones.

2019). Unfortunately, the mixture model was not able to recover its galaxy content, within the criteria we have established to guarantee a high level of confidence in galaxy classification.

We have advanced in our comprehension of the structure and kinematics of the Hercules supercluster, providing an updated description of the system with new ingredients. To finalize, we stress that it consists of a promising target for the mapping of hot gas along the field, including a filament connecting two clusters. A weak lensing study is also required to provide a detailed map of the mass distribution through the field and determine the cluster masses with more precision. Both pieces of information can then be used as input to a tailor-made large-scale hydrodynamical simulation in order to describe the details of the supercluster's formation.

## 8 SUMMARY

We summarize the main findings of this work as follows.

(i) The caustic mass, as well those estimated based on the velocity dispersion, is biased through the cluster merger stage, as it increases over a short period. This fact is not in line with the caustic principle that the technique is not dependent on the cluster dynamical state, even though both techniques provided comparable estimates with our data.

(ii) A2147 ( $\bar{z} = 0.0365 \pm 0.0032$ ) is a bimodal cluster having a total mass of  $13.5_{-1.7}^{+2.1} \times 10^{14} M_\odot$ ; it is probably being observed after pericentric passage.

(iii) A2151 ( $\bar{z} = 0.0361 \pm 0.0024$ ; the Hercules cluster) is composed by five subclusters with a total mass of  $2.88_{-0.27}^{+0.31} \times 10^{14} M_\odot$ ; it is in an early stage of a merger.

(iv) A2152 ( $\bar{z} = 0.0445 \pm 0.0012$ ) is comprised by (at least) two subclusters having a total mass of  $0.72_{-0.10}^{+0.13} \times 10^{14} M_\odot$ .

(v) The core of the Hercules supercluster is constituted by A2147, A2151, and A2152. We found two other galaxy clusters gravitationally bound with this core, increasing the number of known members.

(vi) The total mass of the Hercules supercluster is estimated to be  $2.1 \pm 0.2 \times 10^{15} M_\odot$ .

## ACKNOWLEDGEMENTS

We thank the referee for constructive comments on this work. VMS acknowledges a CAPES scholarship through the grants 88887.508643/2020-00. ALBR is thankful for the support of CNPq, grant 311932/2017-7. RRdC acknowledges financial support from FAPESP through the grant #2014/11156-4.

Funding for the Sloan Digital Sky Survey IV has been provided by the Alfred P. Sloan Foundation, the US Department of Energy Office of Science, and the Participating Institutions.

SDSS-IV acknowledges support and resources from the Center for High Performance Computing at the University of Utah. The SDSS website is [www.sdss.org](http://www.sdss.org).

SDSS-IV is managed by the Astrophysical Research Consortium for the Participating Institutions of the SDSS Collaboration, including the Brazilian Participation Group, the Carnegie Institution for Science, Carnegie Mellon University, Center for Astrophysics, Harvard & Smithsonian, the Chilean Participation Group, the French Participation Group, Instituto de Astrofísica de Canarias, The Johns Hopkins University, Kavli Institute for the Physics and Mathematics of the Universe (IPMU) / University of Tokyo, the Korean Participation Group, Lawrence Berkeley National Laboratory, Leibniz Institut für Astrophysik Potsdam (AIP), Max-Planck-Institut für Astronomie (MPIA Heidelberg), Max-Planck-Institut für Astrophysik (MPA Garching), Max-Planck-Institut für Extraterrestrische Physik (MPE), National Astronomical Observatories of China, New Mexico State University, New York University, University of Notre Dame, Observatório Nacional / MCTI, The Ohio State University, Pennsylvania State University, Shanghai Astronomical Observatory, United Kingdom Participation Group, Universidad Nacional Autónoma de México, University of Arizona, University of Colorado Boulder, University of Oxford, University of Portsmouth, University of Utah, University of Virginia, University of Washington, University of Wisconsin, Vanderbilt University, and Yale University.

The Equatorial Red Atlas of the southern sky was produced using the UK Schmidt Telescope. Plates from this survey have been digitized and compressed by the STScI. The digitized images are copyright (c) 1992–1995, jointly by the UK SERC/PPARC (Particle Physics and Astronomy Research Council, formerly Science and Engineering Research Council) and the Anglo-Australian Telescope Board, and are distributed herein by agreement. All Rights Reserved.

This research has made use of the NASA/IPAC Extragalactic Database, which is funded by the National Aeronautics and Space Administration and operated by the California Institute of Technology.

This work made use of data from the Galaxy Cluster Merger Catalog (<http://gcmc.hub.yt>).

## DATA AVAILABILITY

The data underlying this article will be made available under request to the corresponding author.

## REFERENCES

- Agulli I., Aguerri J. A. L., Dominguez Palmero L., Diaferio A., 2016, *MNRAS*, 461, L6  
 Andrade-Santos F. et al., 2015, *ApJ*, 803, 108  
 Babyk I. V., Del Popolo A., Vavilova I. B., 2014, *Astron. Rep.*, 58, 587  
 Bagchi J., Sankhyayan S., Sarkar P., Raychaudhury S., Jacob J., Dabhade P., 2017, *ApJ*, 844, 25  
 Barmby P., Huchra J. P., 1998, *AJ*, 115, 6  
 Beers T. C., Geller M. J., Huchra J. P., 1982, *ApJ*, 257, 23  
 Bird C. M., Davis D. S., Beers T. C., 1995, *AJ*, 109, 920  
 Bird C. M., Dickey J. M., Salpeter E. E., 1993, *ApJ*, 404, 81  
 Biviano A., Murante G., Borgani S., Diaferio A., Dolag K., Girardi M., 2006, *A&A*, 456, 23  
 Blakeslee J. P., Metzger M. R., Kuntschner H., Côté P., 2001, *AJ*, 121, 1  
 Blanton M. R. et al., 2005, *AJ*, 129, 2562  
 Brinchmann J., Charlot S., White S. D. M., Tremonti C., Kauffmann G., Heckman T., Brinkmann J., 2004, *MNRAS*, 351, 1151  
 Brüggen M., van Weeren R. J., Röttgering H. J. A., 2012, *MNRAS*, 425, L76  
 Canning R. E. A. et al., 2017, *MNRAS*, 464, 2896  
 Chadayammuri U., ZuHone J., Nulsen P., Nagai D., Felix S., Andrade-Santos F., King L., Russell H., 2021, preprint ([arXiv:2108.05296](https://arxiv.org/abs/2108.05296))  
 Chiu I. N., Umetsu K., Murata R., Medezinski E., Oguri M., 2020, *MNRAS*, 495, 428  
 Chon G., Böhringer H., 2015, *A&A*, 574, A132  
 Chon G., Böhringer H., Dasadia S., Kluge M., Sun M., Forman W. R., Jones C., 2019, *A&A*, 621, A77  
 Chon G., Böhringer H., Nowak N., 2013, *MNRAS*, 429, 3272  
 Chow-Martínez M., Andernach H., Caretta C. A., Trejo-Alonso J. J., 2014, *MNRAS*, 445, 4073  
 Cooke B. A., Maccacaro T., Perola G. C., Tarenghi M., Valentijn E. A., 1977, *A&A*, 58, L17  
 Dawson W. A., 2013, *ApJ*, 772, 131  
 de Carvalho R. R., Ribeiro A. L. B., Stalder D. H., Rosa R. R., Costa A. P., Moura T. C., 2017a, *AJ*, 154, 96  
 de Carvalho R. R., Ribeiro A. L. B., Stalder D. H., Rosa R. R., Costa A. P., Moura T. C., 2017b, *AJ*, 154, 96  
 Diaferio A., 1999, *MNRAS*, 309, 610  
 Diaferio A., Geller M. J., 1997, *ApJ*, 481, 633  
 Diaferio A., Geller M. J., Rines K. J., 2005, *ApJ*, 628, L97  
 Doubrava L., Machado R. E. G., Laganá T. F., Lima Neto G. B., Monteiro-Oliveira R., Cypriano E. S., 2020, *MNRAS*, 495, 2022  
 Douglass E. M., Blanton E. L., Randall S. W., Clarke T. E., Edwards L. O. V., Sabry Z., ZuHone J. A., 2018, *ApJ*, 868, 121  
 Dressler A., 1980, *ApJ*, 236, 351  
 Duffy A. R., Schaye J., Kay S. T., Dalla Vecchia C., 2008, *MNRAS*, 390, L64  
 Einasto J., Hütsi G., Suhonenko I., Liivamägi L. J., Einasto M., 2021, *A&A*, 647, A17  
 Einasto M. et al., 2015, *A&A*, 580, A69  
 Einasto M., Tago E., Jaaniste J., Einasto J., Andernach H., 1997, *A&AS*, 123, 119  
 Escalera E., Biviano A., Girardi M., Giuricin G., Mardirossian F., Mazure A., Mezzetti M., 1994, *ApJ*, 423, 539  
 Evrard A. E. et al., 2008, *ApJ*, 672, 122  
 Ferragamo A., Rubiño-Martín J. A., Betancort-Rijo J., Munari E., Sartoris B., Barrena R., 2020, *A&A*, 641, A41  
 Flin P., Krywult J., 2006, *A&A*, 450, 9  
 Foëx G., Chon G., Böhringer H., 2017, *A&A*, 601, A145  
 Geller M. J., Diaferio A., Rines K. J., Serra A. L., 2013, *ApJ*, 764, 58  
 Gifford D., Miller C., Kern N., 2013, *ApJ*, 773, 116  
 Guglielmo V. et al., 2018, *A&A*, 620, A15  
 Gunn J. E., Gott J., Richard I., 1972, *ApJ*, 176, 1  
 Guth A. H., Pi S. Y., 1982, *Phys. Rev. Lett.*, 49, 1110  
 Huang Z., Sarazin C. L., 1996, *ApJ*, 461, 622  
 Hudson D. S., Mittal R., Reiprich T. H., Nulsen P. E. J., Andernach H., Sarazin C. L., 2010, *A&A*, 513, A37  
 Ichikawa K. et al., 2013, *ApJ*, 766, 90  
 Johnston K. V., Sigurdsson S., Hernquist L., 1999, *MNRAS*, 302, 771  
 Käfer F., Finoguenov A., Eckert D., Sanders J. S., Reiprich T. H., Nandra K., 2019, *A&A*, 628, A43  
 Kaiser N., 1987, *MNRAS*, 227, 1  
 Kass R. E., Raftery A. E., 1995, *Journal of the American Statistical Association*, 90, 773  
 Kelkar K. et al., 2020, *MNRAS*, 496, 442  
 Kim J. et al., 2021, preprint ([arXiv:2106.00031](https://arxiv.org/abs/2106.00031))  
 Krause M. O., Ribeiro A. L. B., Lopes P. A. A., 2013, *A&A*, 551, A143  
 Kravtsov A. V., Borgani S., 2012, *ARA&A*, 50, 353  
 Laganá T. F., Durret F., Lopes P. A. A., 2019, *MNRAS*, 484, 2807  
 Laine S., van der Marel R. P., Lauer T. R., Postman M., O'Dea C. P., Owen F. N., 2003, *AJ*, 125, 478  
 Lau E. T., Nagai D., Kravtsov A. V., Vikhlinin A., Zentner A. R., 2012, *ApJ*, 755, 116  
 Lopes de Oliveira R., Carrasco E. R., Mendes de Oliveira C., Bortoletto D. R., Cypriano E., Sodré L. J., Lima Neto G. B., 2010, *AJ*, 139, 216  
 Lopes P. A. A., de Carvalho R. R., Kohl-Moreira J. L., Jones C., 2009, *MNRAS*, 399, 2201  
 Lourenço A. C. C. et al., 2020, *MNRAS*, 498, 835

- Maccagni D., Garilli B., Tarenghi M., 1995, *AJ*, 109, 465  
 Machado R. E. G., Lima Neto G. B., 2013, *MNRAS*, 430, 3249  
 Machado R. E. G., Monteiro-Oliveira R., Lima Neto G. B., Cypriano E. S., 2015, *MNRAS*, 451, 3309  
 Magri C., Haynes M. P., Forman W., Jones C., Giovanelli R., 1988, *ApJ*, 333, 136  
 Mandal S. et al., 2019, *A&A*, 622, A22  
 Molnar S. M., Chiu I. N. T., Broadhurst T., Stadel J. G., 2013, *ApJ*, 779, 63  
 Monteiro-Oliveira R., Cypriano E. S., Machado R. E. G., Lima Neto G. B., Ribeiro A. L. B., Sodré L., Dupke R., 2017a, *MNRAS*, 466, 2614  
 Monteiro-Oliveira R., Cypriano E. S., Vitorelli A. Z., Ribeiro A. L. B., Sodré L., Dupke R., Mendes de Oliveira C., 2018, *MNRAS*, 481, 1097  
 Monteiro-Oliveira R., Doubrava L., Machado R. E. G., Lima Neto G. B., Castejon M., Cypriano E. S., 2020, *MNRAS*, 495, 2007  
 Monteiro-Oliveira R., Lima Neto G. B., Cypriano E. S., Machado R. E. G., Capelato H. V., Lagana T. F., Durret F., Bagchi J., 2017b, *MNRAS*, 468, 4566  
 Monteiro-Oliveira R., Soja A. C., Ribeiro A. L. B., Bagchi J., Sankhyayan S., Candido T. O., Flores R. R., 2021, *MNRAS*, 501, 756  
 More S., Kravtsov A. V., Dalal N., Gottlöber S., 2011, *ApJS*, 195, 4  
 Morell D. F., Ribeiro A. L. B., de Carvalho R. R., Rembold S. B., Lopes P. A. A., Costa A. P., 2020, *MNRAS*, 494, 3317  
 Moura M. T., Machado R. E. G., Monteiro-Oliveira R., 2021, *MNRAS*, 500, 1858  
 Munari E., Biviano A., Borgani S., Murante G., Fabjan D., 2013, *MNRAS*, 430, 2638  
 Navarro J. F., Frenk C. S., White S. D. M., 1996, *ApJ*, 462, 563  
 Navarro J. F., Frenk C. S., White S. D. M., 1997, *ApJ*, 490, 493  
 Ng K. Y., Dawson W. A., Wittman D., Jee M. J., Hughes J. P., Menanteau F., Sifón C., 2015, *MNRAS*, 453, 1531  
 Pandge M. B., Monteiro-Oliveira R., Bagchi J., Simionescu A., Limousin M., Raychaudhury S., 2019, *MNRAS*, 482, 5093  
 Parekh V., Durret F., Padmanabhan P., Pandge M. B., 2017, *MNRAS*, 470, 3742  
 Piffaretti R., Arnaud M., Pratt G. W., Pointecouteau E., Melin J.-B., 2011, *A&A*, 534, A109  
 Pinkney J., Roettiger K., Burns J. O., Bird C. M., 1996, *ApJS*, 104, 1  
 Planck Collaboration et al., 2013, *A&A*, 550, A129  
 Planck Collaboration et al., 2016, *A&A*, 594, A13  
 R Core Team, 2014, R: A Language and Environment for Statistical Computing. R Foundation for Statistical Computing, Vienna, Austria. <http://www.R-project.org/>  
 Regos E., Geller M. J., 1989, *AJ*, 98, 755  
 Ribeiro A. L. B., de Carvalho R. R., Trevisan M., Capelato H. V., La Barbera F., Lopes P. A. A., Schilling A. C., 2013, *MNRAS*, 434, 784  
 Roettiger K., Burns J. O., Loken C., 1996, *ApJ*, 473, 651  
 Rossetti M., Eckert D., De Grandi S., Gastaldello F., Ghizzardi S., Roediger E., Molendi S., 2013, *A&A*, 556, A44  
 Ruggiero R., Machado R. E. G., Roman-Oliveira F. V., Chies-Santos A. L., Lima Neto G. B., Doubrava L., Rodríguez del Pino B., 2019, *MNRAS*, 484, 906  
 Sánchez-Janssen R., Iglesias-Páramo J., Muñoz-Tuñón C., Aguerri J. A. L., Vilchez J. M., 2005, *A&A*, 434, 521  
 Sanderson A. J. R., Ponman T. J., O'Sullivan E., 2006, *MNRAS*, 372, 1496  
 Santiago-Bautista I., Caretta C. A., Bravo-Alfaro H., Pointecouteau E., Andernach H., 2020, *A&A*, 637, A31  
 Sarazin C. L., 2004, *Journal of Korean Astronomical Society*, 37, 433  
 Scaramella R., Baises-Pillastrini G., Chincarini G., Vettolani G., Zamorani G., 1989, *Nature*, 338, 562  
 Schwarz G., 1978, *The Annals of Statistics*, 6, 461  
 Scrucca L., Fop M., Murphy T. B., Raftery A. E., 2016, *The R Journal*, 8, 289  
 Serra A. L., Angus G. W., Diaferio A., 2010, *A&A*, 524, A16  
 Serra A. L., Diaferio A., Murante G., Borgani S., 2011, *MNRAS*, 412, 800  
 Seth R., Raychaudhury S., 2020, *MNRAS*, 497, 466  
 Shapley H., 1934, *MNRAS*, 94, 791  
 Silk J., 1967, *Nature*, 215, 1155  
 Silk J., 1968, *ApJ*, 151, 459  
 Silverman B. W., 1986, Density estimation for statistics and data analysis. Monographs on Statistics and Applied Probability, Chapman and Hall, London  
 Smith A. G., Hopkins A. M., Hunstead R. W., Pimbblet K. A., 2012, *MNRAS*, 422, 25  
 Soja A. C., Sodré L., Monteiro-Oliveira R., Cypriano E. S., Lima Neto G. B., 2018, *MNRAS*, 477, 3279  
 Springel V., Farrar G. R., 2007, *MNRAS*, 380, 911  
 Struble M. F., Rood H. J., 1999, *ApJS*, 125, 35  
 Takizawa M., Nagino R., Matsushita K., 2010, *PASJ*, 62, 951  
 Tarenghi M., Tiffet W. G., Chincarini G., Rood H. J., Thompson L. A., 1979, *ApJ*, 234, 793  
 Tiwari J., Singh K. P., 2021, *MNRAS*, 500, 5524  
 Tucker E., Walker M. G., Mateo M., Olszewski E. W., Geringer-Sameth A., Miller C. J., 2020, *ApJ*, 888, 106  
 Tully R. B., Courtois H., Hoffman Y., Pomarède D., 2014, *Nature*, 513, 71  
 van de Voort F., Bahé Y. M., Bower R. G., Correa C. A., Crain R. A., Schaye J., Theuns T., 2017, *MNRAS*, 466, 3460  
 Vikhlinin A. et al., 2009, *ApJ*, 692, 1033  
 Wang P., Libeskind N. I., Tempel E., Kang X., Guo Q., 2021, *Nature Astronomy*, preprint ([arXiv:2106.05989](https://arxiv.org/abs/2106.05989))  
 Wen Z. L., Han J. L., 2013, *MNRAS*, 436, 275  
 Wojtak R., Łokas E. L., 2007, *MNRAS*, 377, 843  
 Wojtak R., Łokas E. L., Mamon G. A., Gottlöber S., Prada F., Moles M., 2007, *A&A*, 466, 437  
 Yahil A., Vidal N. V., 1977, *ApJ*, 214, 347  
 Yang X., Mo H. J., van den Bosch F. C., Jing Y. P., 2005, *MNRAS*, 356, 1293  
 Yang X., Mo H. J., van den Bosch F. C., Pasquali A., Li C., Barden M., 2007a, *ApJ*, 671, 153  
 Yang X., Mo H. J., van den Bosch F. C., Pasquali A., Li C., Barden M., 2007b, *ApJ*, 671, 153  
 Yu H., Serra A. L., Diaferio A., Baldi M., 2015, *ApJ*, 810, 37  
 Zhang Y. Y., Andernach H., Caretta C. A., Reiprich T. H., Böhringer H., Puchwein E., Sijacki D., Girardi M., 2011, *A&A*, 526, A105  
 ZuHone J. A., Kowalik K., 2016, preprint ([arXiv:1609.04121](https://arxiv.org/abs/1609.04121))